Ocean Modelling 82 (2014) 28–44

Contents lists available at ScienceDirect

Ocean Modelling

journal homepage: www.elsevier.com/locate/ocemod

Eddy-resolving simulations of the Fimbul Ice Shelf cavity circulation: Basal melting and exchange with open ocean

T. Hattermann [a,b,*], L.H. Smedsrud [c], O.A. Nøst [a,b], J.M. Lilly [d], B.K. Galton-Fenzi [e,f]

[a] Norwegian Polar Institute, Fram Centre, Hjalmar Johansens gt. 14, N-9296 Tromsø, Norway
[b] Akvaplan NIVA, Fram Centre, Hjalmar Johansens gt. 14, N-9296 Tromsø, Norway
[c] Geophysical Institute, University of Bergen and Bjerknes Centre for Climate Research, Allégaten 70, 5007 Bergen, Norway
[d] NorthWest Research Associates, PO Box 3027, Bellevue, WA 98009, USA
[e] Australian Antarctic Division, Channel Highway, Kingston, Tasmania 7050, Australia
[f] Antarctic Climate & Ecosystems Cooperative Research Centre, University of Tasmania, Private Bag 80, Hobart, Tasmania 7001, Australia

ARTICLE INFO

Article history:
Received 26 February 2014
Received in revised form 14 July 2014
Accepted 20 July 2014
Available online 7 August 2014

Keywords:
Ice/ocean interaction
Continental shelf/slope exchange
Antarctic Slope Front processes
Fimbul Ice Shelf basal melting
Eddy overturning
Mesoscale ocean modeling

ABSTRACT

Melting at the base of floating ice shelves is a dominant term in the overall Antarctic mass budget. This study applies a high-resolution regional ice shelf/ocean model, constrained by observations, to (i) quantify present basal mass loss at the Fimbul Ice Shelf (FIS); and (ii) investigate the oceanic mechanisms that govern the heat supply to ice shelves in the Eastern Weddell Sea. The simulations confirm the low melt rates suggested by observations and show that melting is primarily determined by the depth of the coastal thermocline, regulating deep ocean heat fluxes towards the ice. Furthermore, the uneven distribution of ice shelf area at different depths modulates the melting response to oceanic forcing, causing the existence of two distinct states of melting at the FIS. In the simulated present-day state, only small amounts of Modified Warm Deep Water enter the continental shelf, and ocean temperatures beneath the ice are close to the surface freezing point. The basal mass loss in this so-called state of "shallow melting" is mainly controlled by the seasonal inflow of solar-heated surface water affecting large areas of shallow ice in the upper part of the cavity. This is in contrast to a state of "deep melting", in which the thermocline rises above the shelf break depth, establishing a continuous inflow of Warm Deep Water towards the deep ice. The transition between the two states is found to be determined by a complex response of the Antarctic Slope Front overturning circulation to varying climate forcings. A proper representation of these frontal dynamics in climate models will therefore be crucial when assessing the evolution of ice shelf basal melting along this sector of Antarctica.
© 2014 The Authors. Published by Elsevier Ltd. This is an open access article under the CC BY license (http://creativecommons.org/licenses/by/3.0/).

1. Introduction

Understanding the interaction of ice shelves with the ocean is a major challenge when assessing the role of Antarctica in a future, almost certainly warmer, climate system (Mercer, 1978; Joughin et al., 2012). Floating ice shelves are believed to buttress the flow of the grounded ice sheet (Rignot et al., 2004; Dupont and Alley, 2005), and recent examples of sudden ice shelf break-up events along the Antarctic Peninsula (Scambos et al., 2000), as well as the rapid mass loss in western Antarctica (Rignot et al., 2008), have raised concerns about the ice/ocean system being highly sensitive to climate change.

The vast majority of ice lost from Antarctica enters the ocean through ice shelves either via iceberg calving or melting at the ice shelf/ocean interface (Jacobs et al., 1992; Rignot et al., 2013). The largest oceanic heat source for driving basal melting originates from the relatively warm, mid-depth Southern Ocean waters that interact with the colder coastal waters across narrow fronts along the continental shelf break. In West Antarctica, these warm waters are observed directly inside the ice shelf cavities (Jenkins et al., 2010), and there is growing evidence that the observed increased glacial mass loss may have been triggered by increased access of warm water onto the continental shelf (Pritchard et al., 2012; Jacobs et al., 2011). In East Antarctica, such a deep ocean heat transport is believed to be much weaker at present (Nicholls et al., 2009), although the continental-scale warming simulations of Hellmer et al. (2012) and Kusahara and Hasumi (2013) suggest that future circulation changes may increase basal melting on decadal time scales also in this region.

* Corresponding author at: Akvaplan-niva, Fram Centre, Hjalmar Johansens gt. 14, N-9296 Tromsø, Norway.
E-mail address: tore.hattermann@akvaplan.niva.no (T. Hattermann).

http://dx.doi.org/10.1016/j.ocemod.2014.07.004
1463-5003/© 2014 The Authors. Published by Elsevier Ltd.
This is an open access article under the CC BY license (http://creativecommons.org/licenses/by/3.0/).

Here, we use a regional high-resolution ice shelf/ocean model, informed by recent sub-ice shelf observations, to investigate basal melting at the Fimbul Ice Shelf (FIS). The oceanographic configuration of the FIS, illustrated by the schematic cross-section in Fig. 1, is typical for the ice shelves along the coast of Dronning Maud Land (40°W–20°E), where ice shelves cover large parts of the narrow continental shelf. Basal melting in this region is believed to be largely determined by the dynamics of the Antarctic Slope Front (ASF), which circulates westward along the steep continental slope (Chavanne et al., 2010; Heywood et al., 1998) and separates the Warm Deep Water (WDW) in the deep ocean off-shore from the colder and fresher Eastern Shelf Water (ESW) on the continental shelf (Nicholls et al., 2009).

Previous coarse-resolution models have suggested the direct inflow of WDW and high melt rates in the order of several meters per year at the FIS (Timmermann et al., 2012; Smedsrud et al., 2006; Hellmer, 2004). Meanwhile, observations indicate much less access of WDW (Nicholls et al., 2006; Price et al., 2008; Walkden et al., 2009), showing that the ice shelf cavity is mainly filled with cold water closely matching the properties of the ESW (Hattermann et al., 2012). Nøst et al. (2011) argue, based on the analysis of hydrographic data collected by instrumented seals in combination with idealized numerical modeling, that baroclinic eddies play an important role for the WDW transport towards the coast. Nøst et al. (2011) find that the coastal thermocline depth is controlled by the balance between a wind-driven Ekman overturning circulation that accumulates ESW near the coast (Heywood et al., 2004; Sverdrup, 1953), and an eddy-driven overturning circulation, which counteracts the deepening of isopycnals across the ASF. Thus, one hypothesis motivating our study is that previous coarse resolution models were not able to realistically simulate basal melting at the FIS because they did not properly represent eddy processes.

In addition, the recent sub-ice shelf observations of Hattermann et al. (2012) showed that fresh and solar-heated Antarctic Surface Water (ASW) has access to the cavity beneath the FIS. This buoyant water mass forms within a thin layer at the ocean surface during the sea ice melt season. The subduction of ASW near the ice front is a typical feature observed along the Eastern Weddell Sea coast (Ohshima et al., 1996; Årthun et al., 2012; Graham et al., 2013). Our work explores the role of ASW and upper ocean processes in basal melting, which has received little attention in the literature to date.

In order to estimate FIS basal melting and to investigate the mechanisms governing basal melting in the Eastern Weddell Sea, a semi-idealized and process-oriented model is constructed, that is capable of generating a realistic sub-ice shelf circulation, while remaining simple enough to be described with only a few parameters. Consistent with satellite observations, the present-day melt rates from our eddy-resolving simulations are considerably lower than suggested by earlier coarse-resolution models, and experiments with varying climate forcing provide new insights into the mechanisms that regulate basal melting in this sector of East Antarctica. New findings of our study are the existence of two distinct states of melting, and the effect of the ice thickness distribution which modulates the melting response at the FIS.

2. Background and data

This section briefly presents the different datasets used to set up and validate our simulations of the FIS cavity circulation.

2.1. Fimbul Ice Shelf geometry

Because the circulation and water mass exchange inside the ice shelf cavity directly relates to ice shelf draft and bedrock topography, we briefly introduce the geometrical configuration of the FIS. Fig. 2(a) shows a map of the FIS region between 2.8°W and 7.6°E—within the two vertical lines—as well as a depiction of the re-entrant channel model domain described later. The topography in the realistic central portion of the model domain is based on the global one-minute RTopo-1 dataset (Timmermann et al., 2010), incorporating bathymetric and ice draft data from a seismic survey on the FIS (Nøst, 2004). The ice draft and grounding line position of the RTopo-1 dataset were refined based on ice-penetrating radar data (Humbert, 2010), as well as by using new ground-based and satellite observations acquired during the

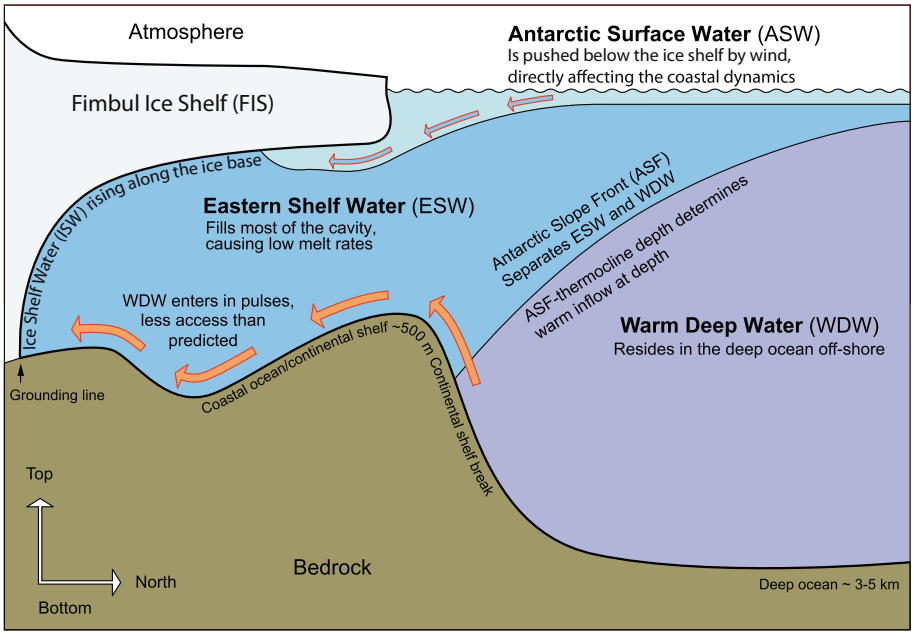

Fig. 1. A schematic cross section of the Fimbul Ice Shelf configuration, illustrating the water masses and processes controlling basal melting along the Eastern Weddell Sea coast.

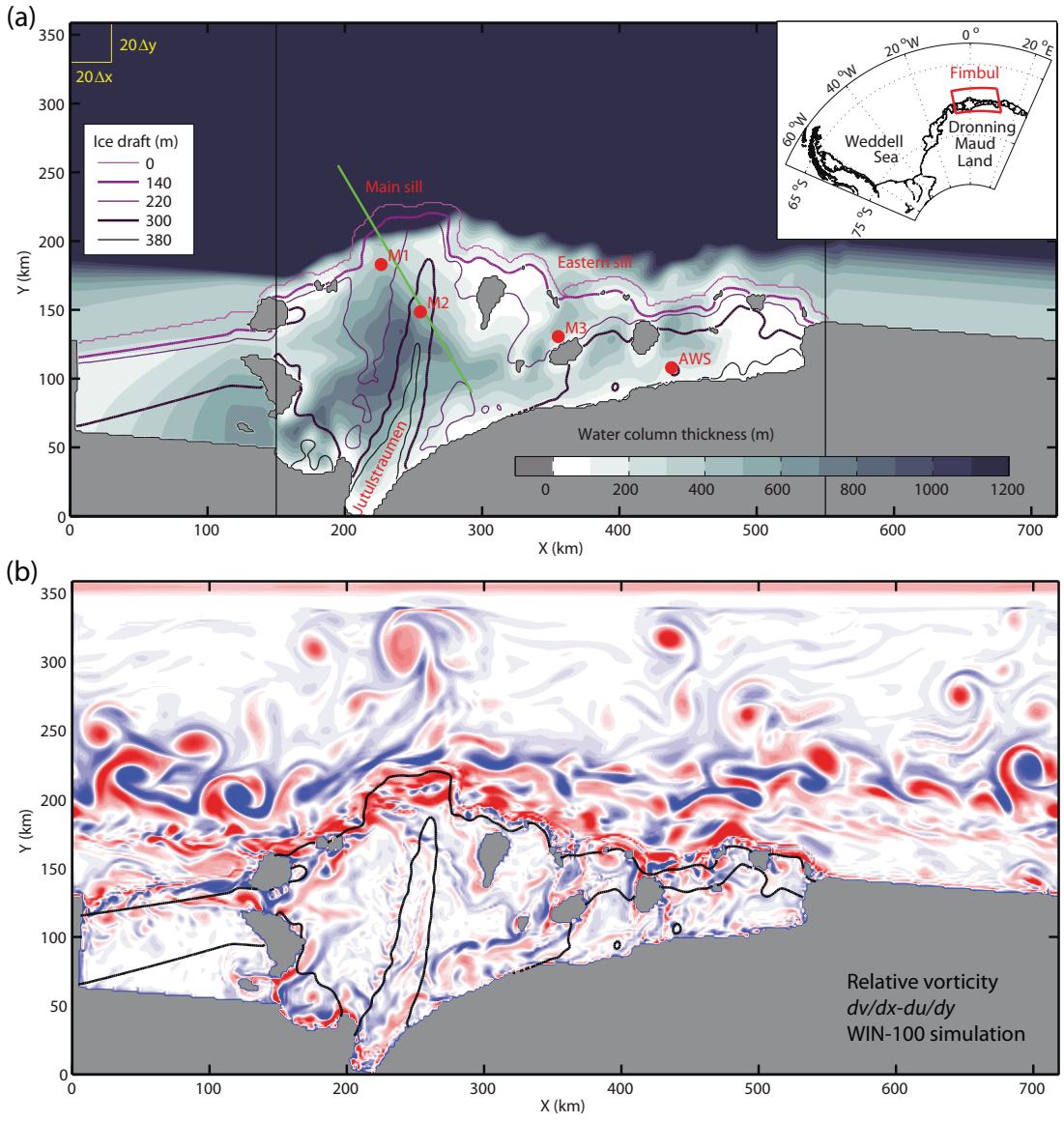

Fig. 2. (a) A map of water column thickness (color shading) and ice draft (contours) within the model domain as described in the text. Areas of grounded ice are shown in gray. The square in the upper left indicates the area covered by 20 × 20 model grid cells. The green line indicates the position of the cross section presented in Fig. 8. The inset in the upper right indicates geographical location of the model domain. (b) A snapshot of relative vorticity for the initialization simulation with WIN-100 forcing. (For interpretation of the references to color in this figure legend, the reader is referred to the web version of this article.)

Norwegian Antarctic Fimbul-Top-to-Bottom Research Expedition during the austral summer season 2009/10.

The most prominent feature of the FIS is the thick body of the Jutulstraumen ice stream that becomes afloat at 71.8°S, and extends northward from about $x = 200$ km in Fig. 2. The rather deep seabed beneath this thick keel of ice forms the central basin of the ice shelf cavity, with a water column thickness of up to 1000 m. East of the central basin, the main expanse of the FIS presents a more horizontally uniform ice thickness of roughly 300 m with a water column thickness beneath seldom exceeding 500 m. North of the ice front, the roughly 500 m deep continental shelf drops into the deep ocean, generally exceeding 2000 m depth. Most of the exchange between the cavity and the open ocean is believed to occur across the main sill and the eastern sill, which are the deepest connections to the interior of the cavity (Nicholls et al., 2006). It is also notable that a portion of the Jutulstraumen ice tongue overhangs the shelf break, permitting it to interact with the coastal current (Walkden et al., 2009).

2.2. Antarctic Slope Front hydrography

Existing large-scale models are presently not sufficiently resolving the ASF dynamics to provide reliable boundary conditions for our high-resolution regional simulations. Instead, we use two complementary datasets to construct a simplified annual climatology of the coastal hydrography for the model forcing and boundary conditions. The cross-sectional structure of the ASF is provided by 26 closely spaced (about 3 km) conductivity-temperature-depth (CTD) profiles, taken across the Eastern Weddell Sea continental shelf break at 17°W (Nøst and Lothe, 1997), and referred to as the NARE section hereafter. The section of potential temperature from these data (Fig. 3(a)) shows a southward deepening thermocline that intersects the continental shelf at about 600 m depth, separating the ESW and WDW. The difference between the two water masses is also seen in the potential temperature-salinity (θ–S) diagram in Fig. 3(b). In this figure, ESW with temperatures near the surface freezing point (about −1.9 °C) and WDW with

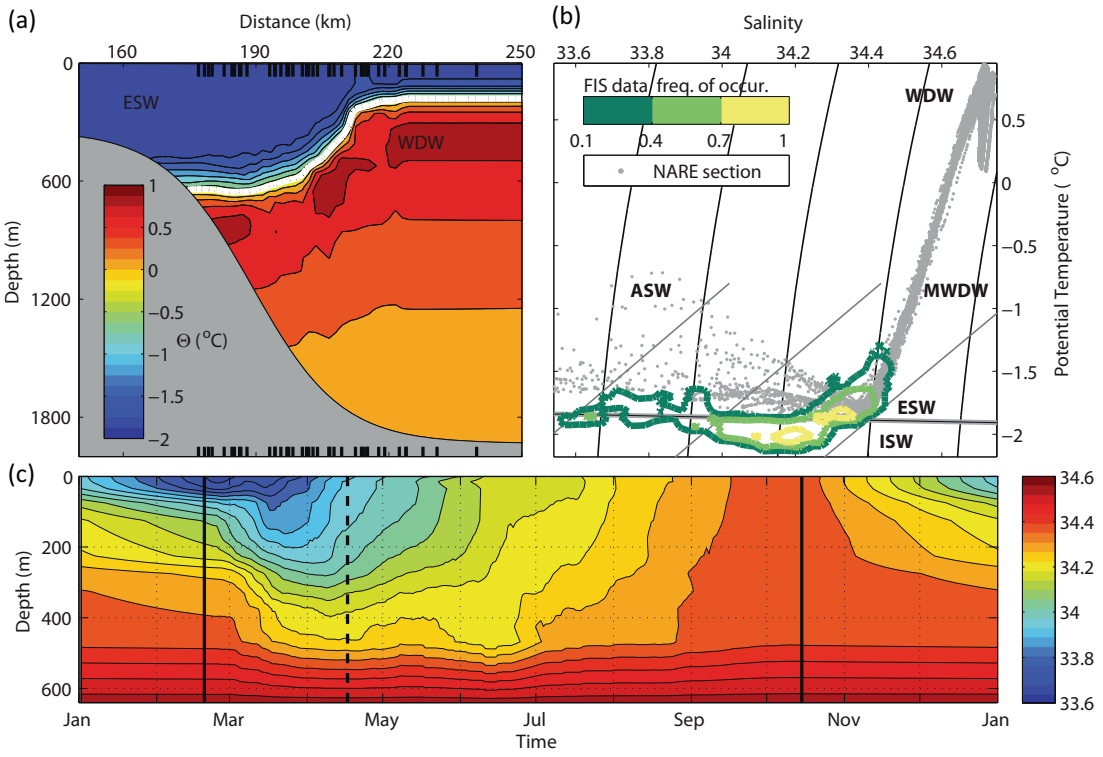

Fig. 3. An overview of the water masses on the Eastern Weddell Sea continental shelf (see Fig. 1 for water mass abbreviations). (a) Shows potential temperature from the NARE section taken across the ASF at 17°W. Black ticks mark profile locations and the white 0.3 °C isotherm indicates the sloping thermocline. (b) Potential temperature-salinity diagram comparing the water masses in the NARE section (gray dots) with the sub-ice shelf observations below the FIS. Colored contours show the relative frequency of occurrence of different water masses beneath the FIS, binned in Θ–S space as described in the text, with yellow shading indicating the most frequently occurring bins on a logarithmic color scale. Sloping gray lines indicate the melt water mixing lines (Gade, 1979) while the horizontal line corresponds to the surface freezing point. Contours of constant potential density are drawn in black. (c) Depth/time slice of the upper ocean hydrographic climatology that is used for the model forcing. The period between the vertical lines is captured by the seal data, with a linear interpolation applied outside of these lines. The dashed line indicates the situation that is taken for the constant summer forcing scenario. (For interpretation of the references to color in this figure legend, the reader is referred to the web version of this article.)

temperatures of +0.9 °C appear as two endpoints joined by a straight line. This mixing product of the ASF pycnocline is known as Modified Warm Deep Water (MWDW). Being collected during the austral summer, the NARE section also illustrates the properties of the fresh, near surface ASW, which is the most buoyant water mass with temperatures of up to −1 °C in Fig. 3(b).

In addition, a set of more than 2000 CTD profiles collected by instruments affixed to southern elephant seals, presented by Nøst et al. (2011) and referred to as seal data hereafter, gives a unique sample of the seasonal evolution of the water masses along the coast. The seal data and the NARE section are combined to construct a time-dependent version of the ASF cross-section. In this construction, water mass properties below the thermocline, here defined as the 0.3 °C isotherm, are given by the NARE section and remain constant in time. The upper-ocean properties are provided by a time series of the horizontally averaged seal data. To assure a smooth transition between the two datasets, the hydrographic properties at the vertical interface have been interpolated over a constant thermocline thickness of 70 m, obtained by analyzing the seal data, and with corrections applied to preserve realistic properties of the MWDW. The resulting depth/time section of upper ocean salinity in Fig. 3(c) reveals a pattern of summertime near-surface freshening, followed by a vertical homogenization due to the salinification from brine rejection during sea ice formation in winter.

The NARE section prescribing deep ocean properties in our climatology is located several hundred kilometers west of our study region. However, a comparison with both the CTD profiles taken near the FIS, and with the seal data, shows that the assumption of constant deep ocean properties along the Eastern Weddell Sea coast is a reasonable first-order approximation for our process-oriented model setup.

2.3. Coastal wind field

The main driver of the mean circulation along the Eastern Weddell Sea coast is the mechanical surface forcing due to prevailing easterly winds (Nunez-Riboni and Fahrbach, 2009). Here, we use results from the high resolution (27 km) Antarctic Ice Sheet Regional Atmospheric Climate Model (RACMO2) of Lenaerts et al. (2012) to derive a simplified wind forcing for our model. For this derivation, the RACMO2 data is compared to observations from an automatic weather station (AWS) that was operational from January 2010 to January 2012 on the FIS at the location indicated in Fig. 2(a). Fig. 4(a) shows the time series of the 48-h low-pass filtered zonal wind component obtained from the AWS together with the atmospheric simulations (interpolated to the same location) that were available at the time when the simulations for our study were set up. RACMO2 convincingly captures the timing and magnitude of the major wind events observed on the FIS, whereas more quiet periods and reversing westerly winds are generally less well reproduced by the simulations. Both time series also show a primarily high-frequency variability of the zonal wind stress, with no clear seasonal cycle in wind strength or frequency of storm events (not shown) being apparent during the observational period. We also note that there appears to be no obvious connection between the variability of the winds and the warm pulses seen beneath the FIS apparent in Fig. 4(b), discussed in more detail shortly.

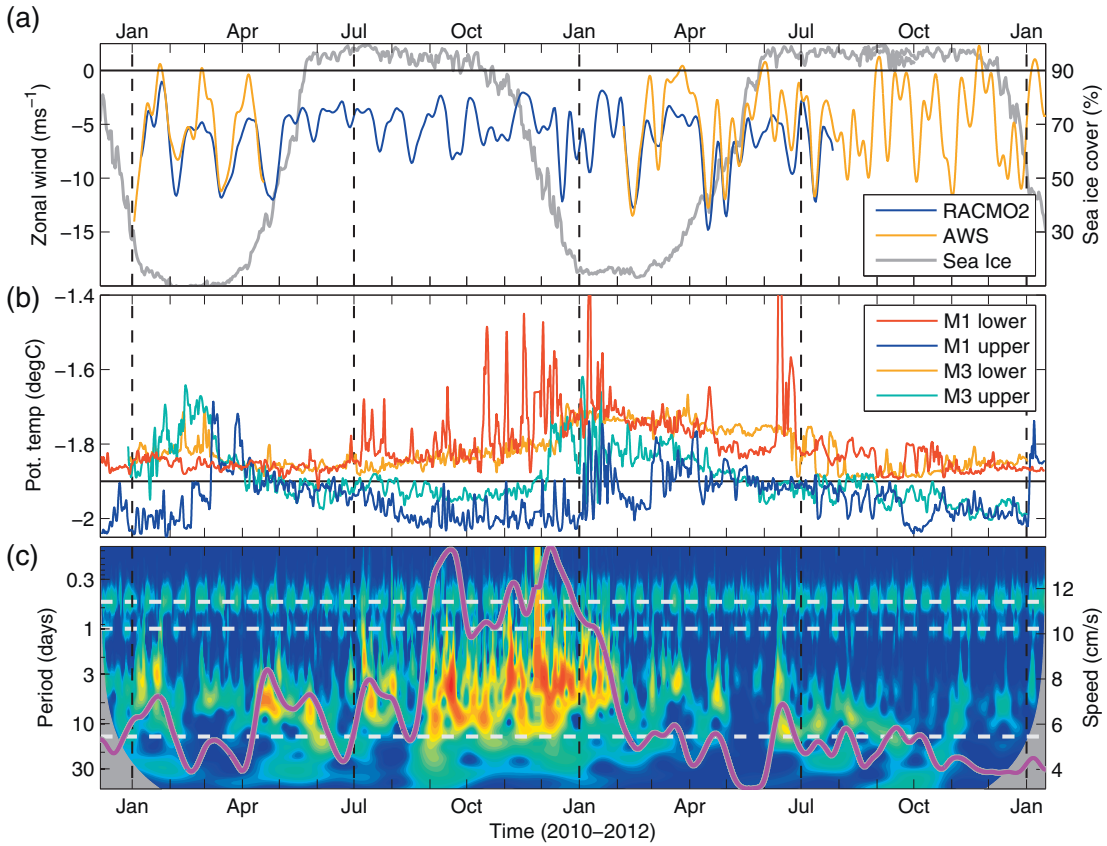

Fig. 4. Observations at the Fimbul Ice Shelf during 2010–2012. Time series of zonal winds (a) from the automatic weather station (AWS) data and the RACMO2 model (left axis) are shown together with average sea ice concentration in the model domain (right axis) as obtained from AMSR-E/SSMIS sea ice maps (Spreen et al., 2008). (b) 48 h low-pass filtered time series of sub-ice shelf potential temperatures at the M1 and M3 mooring that were presented by Hattermann et al. (2012). Panel (c) shows the spectral energy distribution of the currents at the lower sensor of M1 from a wavelet analysis (color shading, left axis), together with 30 day low-pass filtered current speed (magenta curve, right axis). The dashed white lines indicate the periods of the major tidal constituents. (For interpretation of the references to color in this figure legend, the reader is referred to the web version of this article.)

Additional uncertainty in the wind forcing is added by sea ice that modulates the momentum transfer from the atmosphere into the ocean. In the FIS region, only small amounts of land-fast ice, which would entirely block the transfer of momentum onto the ocean surface, are found (Fraser et al., 2012). But also the seasonally varying ice cover, illustrated by the gray line (right axis) in Fig. 4(a) (Spreen et al., 2008), of predominantly drifting ice alters the momentum transfer, possibly introducing seasonal variations to the ASF current strength (Nunez-Riboni and Fahrbach, 2009). This effect is difficult to assess, because ice drift may either increase or decrease the momentum transfer depending on its properties (Lüpkes and Birnbaum, 2005). Thus, the simplest approach for our process-oriented study is to neglect the effect of sea ice and to compute the climatological mean ocean surface stress (τ^u, τ^v) directly from the RACMO2 "2 m" winds (u, v) as

$$\tau^u = \rho_a C_a \sqrt{u^2 + v^2}\, u, \quad \text{and} \quad \tau^v = \rho_a C_a \sqrt{u^2 + v^2}\, v$$

with the density of air being $\rho_a = 1.4\ \mathrm{kg\ m^{-3}}$, and with a drag coefficient of $C_a = 1.3 \times 10^{-3}$ at the air–ocean interface (Smith, 1988). In addition, the model sensitivity to different surface stress fields will be explored by a set of idealized forcings described in Section 3.4.

2.4. Recent sub-ice shelf observations

Essential datasets for evaluating our simulations are provided by Hattermann et al. (2012), who presented sub-ice shelf observations acquired via three hot-water drill holes denoted M1, M2, and M3 in Fig. 2(a) (see supplementary material). The observations consist of a set of two-year time series from six moored current meter instruments, with an upper instrument close to the ice base and a lower instrument near the seabed at each drill hole, and CTD profiles that were taken at each site during the deployment of the moorings. Parts of these data are presented in Figs. 3(b) and 4(b) and (c), showing a histogram of observed θ–S properties at M1 and M2 and time series of potential temperature and current variability at M1 and M3 beneath the ice, respectively.

Hattermann et al. (2012) hypothesized the interplay of three different "Modes" of basal melting (see Jacobs et al., 1992) at the FIS. The yellow contours in Fig. 3(b) show that cold ESW is the most common water mass entering the ice shelf cavity, indicating that basal mass loss is dominated by the "freezing-point depression" Mode 1-type of melting described by Jacobs et al. (1992). In this mode, high melt rates are confined to deeper ice, while ice shelf water (ISW) with temperatures below the surface freezing point ascending from greater depth potentially causes marine ice formation beneath shallower ice (Hellmer and Olbers, 1989; Jenkins, 1991). Furthermore, the observations showed the access of warmer water at different depths that may provide additional heat for melting beneath the FIS. The seasonal access of solar heated surface water may cause a shallow Mode 3-type melting in the upper part of the cavity. This is shown by the slightly higher temperatures during late summer and fall at the upper sensors (blue curves in Fig. 4(b)), as well as by the appearance of a fresher water mass (green contours in Fig. 3(b)) that resembles the ASW seen in the NARE section. At depth, a limited amount of MWDW

appears to enter the cavity across the main sill, potentially providing a deep source of heat for Mode 2-type melting. This is shown by pulses of higher temperatures at the lower sensor of M1 (red curve in Fig. 4 and a θ–S signature (Fig. 3(b)) that resembles the MWDW mixing line connecting the ESW and WDW and maximum temperatures of around −1.3 °C. As opposed to the ESW that is frequently observed at all sensors, the low frequency of occurrence of MWDW and ASW in Fig. 4(b) indicates the intermittent nature of the Mode 2 and Mode 3-type melting, and one goal of our modeling study is to partition the relative importance of these different heat sources for overall basal mass loss at the FIS.

In order to further explore the hypothesis that eddies are important for the deep ocean heat transport, and to provide a further basis for scrutinizing the model results, we extend the analysis of current variability presented by Hattermann et al. (2012) to characterize the warm pulses at depth that are seen in Fig. 4(b). Fig. 4(c) presents the modulus of a wavelet transform,[1] where the color shading indicates the speed associated with velocity fluctuations over the course of the year and having a particular time scale or period (left axis). Comparison of Fig. 4(b) and (c) shows that warm pulses are directly associated with brief instances of enhanced levels of current variability on time scales between three and ten days. Furthermore, the time series of the 30 day low-pass filtered current speed (magenta curve in Fig. 4(c), right axis) shows that the MWDW inflow occurs during periods of stronger background currents. Lilly et al. (2003) find that the contemporaneous occurrence of water mass anomalies, and narrow pulses of enhanced current variability, is a characteristic signature of the advection of coherent eddies past a mooring. Thus, the observed current characteristics associated with the warm pulses at the lower sensor of M1 support the hypothesis of Hattermann et al. (2012) that advection of MWDW across the sill is associated with enhanced mesoscale eddy activity.

3. The Fimbul Ice Shelf/ocean model

We use a modified version of the free-surface, hydrostatic, primitive-equation, terrain-following, Regional Ocean Model System (ROMS) (Shchepetkin and McWilliams, 2005) that has been adapted by Dinniman et al. (2007) to allow the vertical "s-coordinate" to follow the ice shelf draft. Ice shelf/ocean interaction processes are parameterized following Hellmer and Olbers (1989) and are implemented as described by Galton-Fenzi et al. (2012), but omitting the frazil component of the latter work. Fluxes at the ice/ocean boundary are described by three equations representing the conservation of heat and salt, and a linearized version of the freezing point of seawater (as a function of salinity and pressure), which are solved to simultaneously find the temperature and salinity in the boundary layer beneath the ice shelf and the melt rate at the ice shelf base. Exchange coefficients are computed according to Eqs. (11) and (12) in Holland and Jenkins (1999) and using the parameters as suggested in that work. Similar approaches have been used to implement ice shelf/ocean processes into other general circulation models (Hellmer, 2004; Smedsrud et al., 2006; Losch, 2008; Timmermann et al., 2012), and to assure comparability with previous results, the model configuration has been validated (Galton-Fenzi, 2009) based on the ice shelf-ocean model intercomparison project (ISOMIP) described in Hunter (2006). However, the processes controlling basal melting at the ice/ocean interface are subject to ongoing research. For instance the presence of topographical features over a broad range of length scales (Nicholls et al., 2006; Langley et al., 2014) and the effects of basal melt water input from the grounded ice sheet (Jenkins, 2011; Le Brocq et al., 2013) are found to have important effects on basal melting that are not yet captured by most ice shelf/ocean models.

Our model is implemented on an f-plane and does not include a dynamical sea ice component. A simplified version of this model was used by Nøst et al. (2011) to study the effect of the eddy-overturning of the ASF in an idealized channel geometry. All technical aspects not explicitly discussed in this section, such as the applied schemes for time-stepping, vertical mixing, bottom friction, and the equation of state, are identical to those presented by Nøst et al. (2011).

3.1. Model domain and resolution

Following Smedsrud et al. (2006) and Nicholls et al. (2008), we approximate the mean circulation outside the ice shelf cavity by a quasi-steady flow along the continental slope, which motivates the application of a periodic channel geometry. The re-entrant circulation avoids spurious reflections at open boundaries and permits the full evolution of the FIS mesoscale eddy field within a compact model domain. A similar setup was used by Tverberg and Nøst (2009) to study the eddy-driven cross-slope exchange in polar waters, along the coast of Svalbard.

Outside the two vertical lines shown in Fig. 2(a), the model domain, which is 720 km long and 360 km wide, transitions to an idealized cross-channel profile to smoothly join the eastern and western boundaries. In the meridional direction, the domain extends from the southernmost location of the FIS grounding line at the Jutulstraumen ice stream to approximately 150 km north of the continental shelf break.

Various tests with simplified configurations, similar to that presented by Nøst et al. (2011), have shown that growth of baroclinic instabilities within the ASF and the associated cross-shelf exchange are sensitive to model resolution and to the choice of eddy mixing parameters. In agreement with St-Laurent et al. (2013) we find that baroclinic eddies over the continental slope develop when the horizontal grid spacing is in the order of 1 km and the eddy viscosity is kept below about 5 $m^2\,s^{-1}$. Here we use a 1.5 km horizontal grid resolution (480 × 240 grid points) and apply a third-order upwind advection scheme, using no explicit eddy diffusion for either momentum or tracers. This combination was chosen because it appeared to provide the least amount of diffusion, while still assuring numerical stability for our configuration.

The model consists of 24 vertical layers with enhanced resolution close to the surface and near the seabed. The layer thickness varies from 4 m in the thinnest surface layer up to 130 m in the deep ocean interior, with a maximum layer thickness of less than 50 m over the continental slope at ocean depths shallower than 1000 m. The water column thickness at the grounding line is set to a minimum of 100 m, while the maximum ocean depth north of the continental slope was truncated at 2500 m for computational efficiency. In this setup the model runs stably with a baroclinic time steps of 200 s, each with 30 barotropic sub-steps.

3.2. Minimizing pressure gradient force errors

A known issue of terrain-following models such as ROMS is the pressure gradient force error induced by steeply sloping topography (Beckmann and Haidvogel, 1993). In order to minimize this effect, the bathymetry and ice shelf draft were smoothed with a second order Shapiro filter allowing for a maximum grid stiffness between two neighboring grid cells with depths h_{i-1} and h_i of

$$r_x = \frac{|h_{i-1} - h_i|}{h_{i-1} + h_i} \leqslant 0.25.$$

[1] The wavelet used here is the generalized Morse wavelet characterized by parameters $\gamma = 4$ and $\beta = 3$ with normalizations and other details as described by Lilly and Olhede (2009).

The three regions which are impacted the most are the continental slope, the areas near the grounding line, and the vertical ice front. In particular, the smoothing of the ice front, which is necessary to ensure numerical stability of the model, could influence the cavity exchange and the simulated basal melting; the impact of such effects are discussed in more detail in Section 6.2.

Sufficiently small pressure gradient errors are commonly believed to alter the solution by linearly superimposing a geometry-dependent spurious component to the background flow. To assure that these effects are minimized, several tests with various realistically stratified but horizontally uniform profiles of temperature and salinity were performed. In these test cases, which ideally should produce an equilibrium state that is fully at rest, the maximum velocities occur near the ice front, but remain small (below $2\,cm\,s^{-1}$) relative to the typical 5–50 $cm\,s^{-1}$ currents occurring in the full simulation.

3.3. Idealized present-day "ANN-100" forcing

In order to estimate the influence of different oceanic processes on basal melt rates, a set of semi-idealized model forcings is derived from the data presented in Section 2. The forcing which most realistically represents the FIS present-day conditions, referred to as experiment "ANN-100" hereafter, assumes a quasi-steady annual cycle of the coastal circulation and can be described as follows.

To reproduce realistic water masses in the model interior, temperature and salinity at the eastern (inflow) model boundary are nudged to the time-varying climatological ASF section described in Section 2.2. The nudging time-scale varies linearly from 3 days at the boundary to 10 days at the interior end of the 15 grid point wide nudging zone in all 24 vertical layers. A sponge layer with enhanced diffusion of tracers and momentum in the northernmost 10 grid points minimizes reflections at the northern channel wall, and a full-depth nudging of temperature and salinity (with a 30 day time scale) in the sponge layer is applied to preserve a horizontally homogeneous water mass distribution in the deep ocean.

The surface properties outside the FIS are largely determined by the annul cycle of melting and freezing of sea ice (Nicholls et al., 2009). To mimic the effect of sea ice, which is not included in our model, temperature and salinity within the uppermost model layer are directly restored to the horizontally averaged surface climatology obtained from the seal data, with a nudging time scale of 10 days. This setup for the hydrographic forcing avoids the uncertainties associated with poorly constrained fluxes at the air-ice-ocean boundary, and allows us to study the direct oceanic response to different upper ocean conditions, while assuring a consistent model forcing.

For the mechanical surface forcing, a wind stress that is constant in time, but resolves the average spatial pattern of the wind field in the model domain is applied. The forcing field is derived by time-averaging the RACMO2 results, with minor modifications applied in order to ensure periodicity at the boundaries. This time-invariant wind scenario allows us to separate internal variability from the model forcing and was chosen because the wind data shows neither a clear annual cycle nor a direct relation to the warm pulses observed beneath the FIS (Fig. 4). In addition, it is unclear how the temporal and spatial scales of the time-varying wind field would affect the circulation in the limited model domain, possibly causing circulation artifacts due to interference at the periodic boundary.

Another simplification that is required to ensure consistency at the periodic model boundaries is the omission of tidal forcing. Propagating tidal waves would interfere with their images at the cyclic model boundary. Also the successive superposition of tides in separate non-cyclic model runs was found to strongly alter the mean circulation, leading to the development of circulation artifacts (Abrahamsen, 2012). However, tidal currents in the Eastern Weddell Sea region are generally rather weak (Padman et al., 2002). A discussion on how tides, sea ice and time-varying winds may alter our results will be given in Section 6.3.

3.4. Experiments with varying model forcing

In addition to the semi-idealized ANN-100 experiment, we study the melting response to different climatic conditions by systematically varying the idealized model forcing.

The role of easterly winds for the momentum balance of the ASF current is explored by varying the magnitude of the wind stress by a constant factor, here denoted by percentages with "100" indicating the RACMO2 average. A strong wind forcing (denoted "130") with 130% of the average surface stress, as well as four weak wind forcing forcings (30, 40, 60 and 70), are applied. This range was chosen to highlight the two possible states of melting that are revealed by our simulations.

The effect of the ASW formation is investigated by using different hydrographic conditions for the water mass restoring at the surface and the lateral boundaries. In addition to the time-varying annual cycle scenario described above (denoted ANN) a constant summer (SUM) and a constant winter (WIN) scenario are used for the hydrographic nudging. In the constant winter scenario, no ASW is present and a homogeneous layer of ESW with temperatures at the surface freezing point occupies the water column above the thermocline. The constant summer scenario is defined by the mid-April climatology indicated by the dashed line in Fig. 3(c), when the distribution of ASW extends deepest throughout the water column.

Combining the different wind and hydrographic forcings, 18 different experiments, as denoted in Table 1, were preformed. Each experiment starts from an initialization state at equilibrium, produced by a 10 year spin-up with the constant winter (WIN-100) forcing applied and the model being initialized with temperatures at the surface freezing point, a horizontally uniform salinity profile, and zero velocities. The initialization state reproduces a fully developed ASF mesoscale eddy field, as illustrated by the snapshot of relative vorticity in Fig. 2(b). In this state, no warm water enters the ice shelf cavity, allowing discrimination between the effect of individual processes in the different experiments. Each experiment is integrated for five model years with the respective forcing fields applied. Some of these runs approach a new steady state, whereas other simulations—particularly those exhibiting strong inflow of warm water beneath the ice—do not reach a new equilibrium. We chose not to integrate the model for longer time because the ongoing trends in these runs are clear and because the applied forcing is relatively extreme in these scenarios and does not represent typical conditions at the present time.

Table 1
A summary of the model experiments. Letters correspond to the applied hydrographic scenario, while the wind forcing is denoted by numbers, which correspond to the strength of the applied surface stress given in percent relative to the climatological mean.

	Weak wind	Mean wind	Strong wind
Winter hydrography	WIN-30, −40, −60, −70	WIN-100	WIN-130
Annual hydrography	ANN-30, −40, −60, −70	ANN-100	ANN-130
Summer hydrography	SUM-30, −40, −60, −70	SUM-100	SUM-130

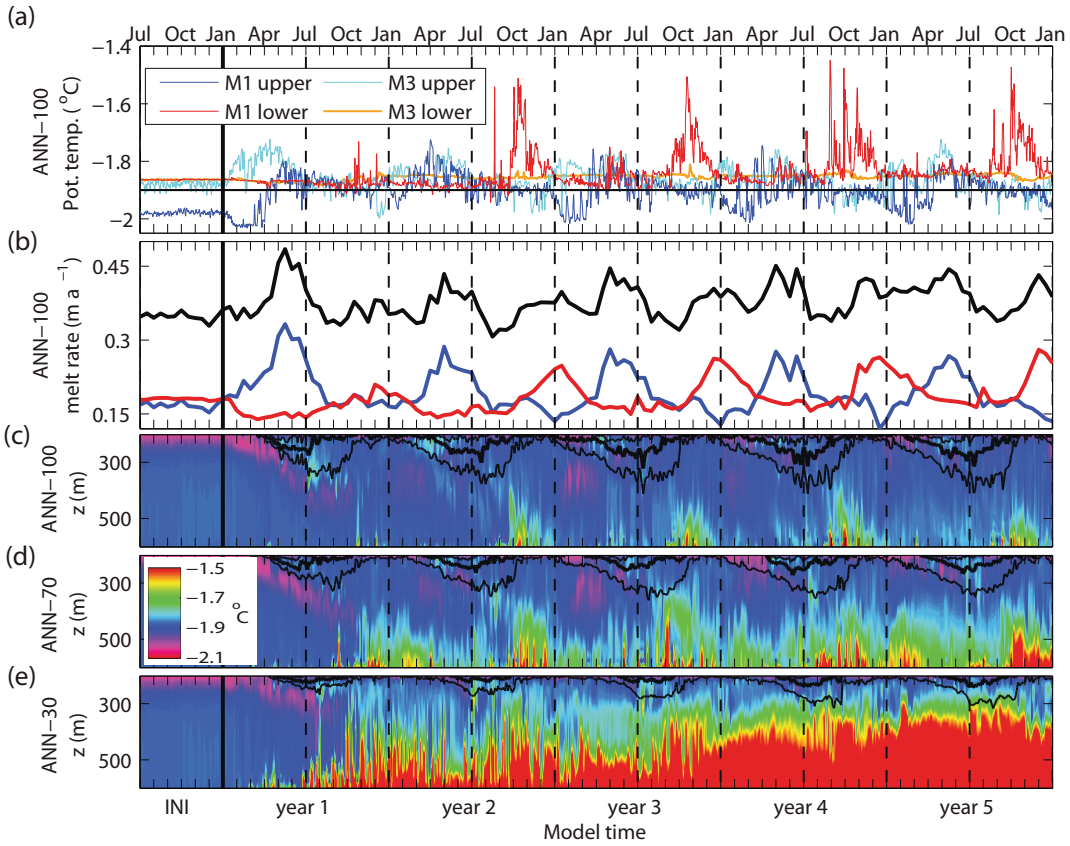

Fig. 5. Model time series of the ANN experiments (a) reproducing the M1 and M3 temperature records shown in Fig. 4, and (b) showing spatially averaged total (black), deep (red) and shallow (blue) melting from the ANN-100 simulation. Panels (c)–(e) show time series of M1 temperature profiles (color shading) and salinity contours (34, 34.1, and 34.2 psu), illustrating the model response to different wind forcings. Prior to the five years of the model experiments, which start when indicated by the thick vertical lines, all time series include the last six months of the initialization simulation (INI) with WIN-100 forcing. (For interpretation of the references to color in this figure legend, the reader is referred to the web version of this article.)

3.5. Model evaluation

We assess the realism of our simulations by comparing the recent observations below the FIS with synthetic mooring data from the most realistic ANN-100 experiment. Together with other parameters presented later, Fig. 5 shows a time series of simulated temperatures (Fig. 5(a)), interpolated at locations of the upper and lower sensors of M1 and M3, covering the five model years of the ANN-100 experiment and the last six months of the initialization simulation. For comparison, the temperature axes in Fig. 5(a) and Fig. 4(b) are equal. In general, the model shows predominantly low ice shelf cavity temperatures and warmer events due to the intermittent access of ASW and MWDW, yielding a sub-ice shelf water mass distribution that resembles the observations. This can be seen from the θ–S histograms in Fig. 6, presenting the frequency of occurrence of different water masses at M1 and M2 in the different model experiments. The color shading uses the same scale as for the observations in Fig. 3(b), which for comparison are overlaid as black contours, showing most similarity with the ANN-100 experiment in Fig. 6(b).

The model reproduces warm pulses of MWDW at the lower sensor of M1 (red curve in Fig. 5(a)), with similar characteristics as observed by the actual M1 mooring in Fig. 4(b). A wavelet analysis of the synthetic mooring time series (not shown) reveals a similar frequency distribution and intensity of the episodes of increased current variability, contemporaneous with warm pulses of deep water, in agreement with the pattern described for the observations in Section 2.4. However, with a strictly periodic seasonal forcing applied, the model shows a regular inflow of MWDW at M1 during late winter and spring, while the two available years of observations suggest a greater inter-annual variability for the warm pulses at depth.

Also the seasonal access of ASW beneath the FIS is reproduced by the model. This is shown by higher temperatures in the period between January and July at the upper sensors of M1 and M3 (blue curves), while temperatures below the surface freezing point indicate the presence of ISW during the rest of the year. To this end, the time lag between the ASW production during sea ice melting in November/December and its arrival at the mooring is consistent with the hypothesis that surface water enters the ice shelf cavity after being downwelled at ice front by on-shore Ekman transport. While the temperature maximum appears to be more delayed in the model, also the two years of observations show different timings, with an earlier arrival of ASW in 2011 (December/January) then in 2010 (February/March). Furthermore, the model and the observations show a consistent time lag of about two months between the arrival of ASW at M1 and M3, likely being caused by the blocking effect of the Jutulstraumen ice tongue that leads to more accumulation of surface water on the eastern side of the FIS (Zhou et al., 2014).

4. Basal melting and circulation in the ANN-100 experiment

The correspondence between the simulations and the sub-ice shelf observations suggests that the model captures the main

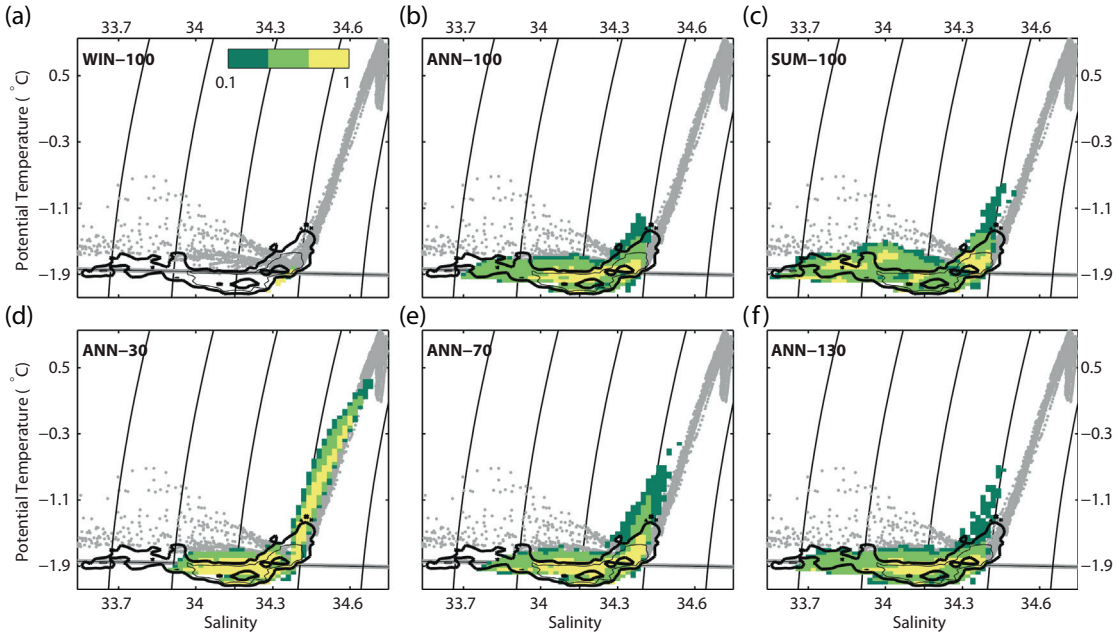

Fig. 6. Sub-ice shelf water mass distribution for different model experiments. The color shading in the Θ–S histograms shows the relative frequency of occurrence of different water masses for the synthetic M1 and M2 time series, using the same logarithmic color scaling, with yellow indicating the most frequently observed water masses, as for the observations in Fig. 3(b) which are here indicated by black contours. Gray dots show CTD profiles of the NARE section. (For interpretation of the references to color in this figure legend, the reader is referred to the web version of this article.)

dynamics of the ice shelf/ocean interaction at the FIS, and we now analyze the characteristics and variability of basal melting in the ANN-100 experiment.

4.1. Average melt rates and spatial melting distribution

A map of temporally-averaged basal melting and freezing rates from the last year of the ANN-100 experiment is shown in Fig. 7(a). Black contours indicate ice draft, with the northernmost border corresponding to the 140 m contour in Fig. 2(a). The area average basal melt rate is about 0.4 m year^{-1}, accounting for a net mass loss of about 14 Gt year^{-1}. Note that for calculating average melt rates in this paper, we omit the ice front region that is attributed to the topographic smoothing described in Section 3.2, and only include ice thicker than 140 m (thick magenta line in Fig. 2(a)). Areas of sloping ice shallower than 140 m, where the simulations show unrealistically high rates of melting and freezing over an artificially enlarged area, account for about 9% of the total ice shelf area in the model, contributing an additional 0.1 m year^{-1} to the average basal mass loss in the ANN-100 experiment. While these model artifacts add considerable uncertainty to the absolute melting estimate in our study, they are of minor importance for the conclusion that our simulations provide a substantially lower estimate than earlier coarse resolution models, which suggested melt rates of a few meters per year for the FIS (Smedsrud et al., 2006; Timmermann et al., 2012). Instead, our results are similar to recent remote sensing based estimates of 0.57 m year^{-1} (Rignot et al., 2013) and consistent with earlier observational studies that suggested generally low basal mass loss at the FIS (Pritchard et al., 2012; Price et al., 2008).

The spatial pattern in Fig. 7(a) shows stronger melting of deeper ice draft, also seen in previous simulations of Smedsrud et al. (2006), but with lower overall magnitudes in our study. In particular along the deep keel of Jutulstraumen, high melt rates of several meters per year occur, while the large uncolored areas in Fig. 7(a) indicate nearly zero melting over most of the ice shelf between 200 m and 300 m depth. Such low melt rates beneath shallow ice support the hypothesis of a dominant Mode 1-type of melting, in which substantial melting only occurs where the increased ocean pressure at greater depth reduces the local freezing point.

Moderate melting of a few meters per year occurs adjacent to the ice front, especially between 1.5°W and 0°E where the ice shelf overhangs the continental shelf break. Enhanced melting in this region was inferred from oceanographic observations (Walkden et al., 2009), and recently this feature, which is consistently seen in modeling studies (Nicholls et al., 2008; Smedsrud et al., 2006), has also been confirmed by remote sensing based (Rignot et al., 2013) and in situ measurements (Langley et al., in preparation) of basal melting at the FIS.

While errors in our simulations are likely to be introduced by the artificially enhanced minimum water column thickness of 100 m at the grounding line, the simulated maximum melt rate of about 15 m year^{-1} in the southernmost part of Jutulstraumen is in good agreement with estimates from glaciological mass flux divergence estimates in this location (Humbert, 2012). Test runs with a more realistic, but numerically less stable water column thickness of 50 m showed only minor variations of the simulated melt rates under forcing conditions similar to the ANN-100 experiment.

Smaller areas of net freezing are also observed, mostly in regions where the buoyant ISW ascends along steeper parts of the ice base and becomes supercooled as it reaches shallower depth. But the amount of freezing contributes less than 5% to the total basal mass balance in the ANN-100 experiment, suggesting that no substantial accretion of marine ice occurs beneath the FIS. However, freezing processes are incomplete, with no frazil ice processes being included in the model.

4.2. Seasonal variability of deep and shallow melting

The ANN-100 experiment features a seasonality of basal melt rates that suggests a distinct contribution of melting at different depths beneath the FIS. In order to illustrate this, Fig. 7(b) and

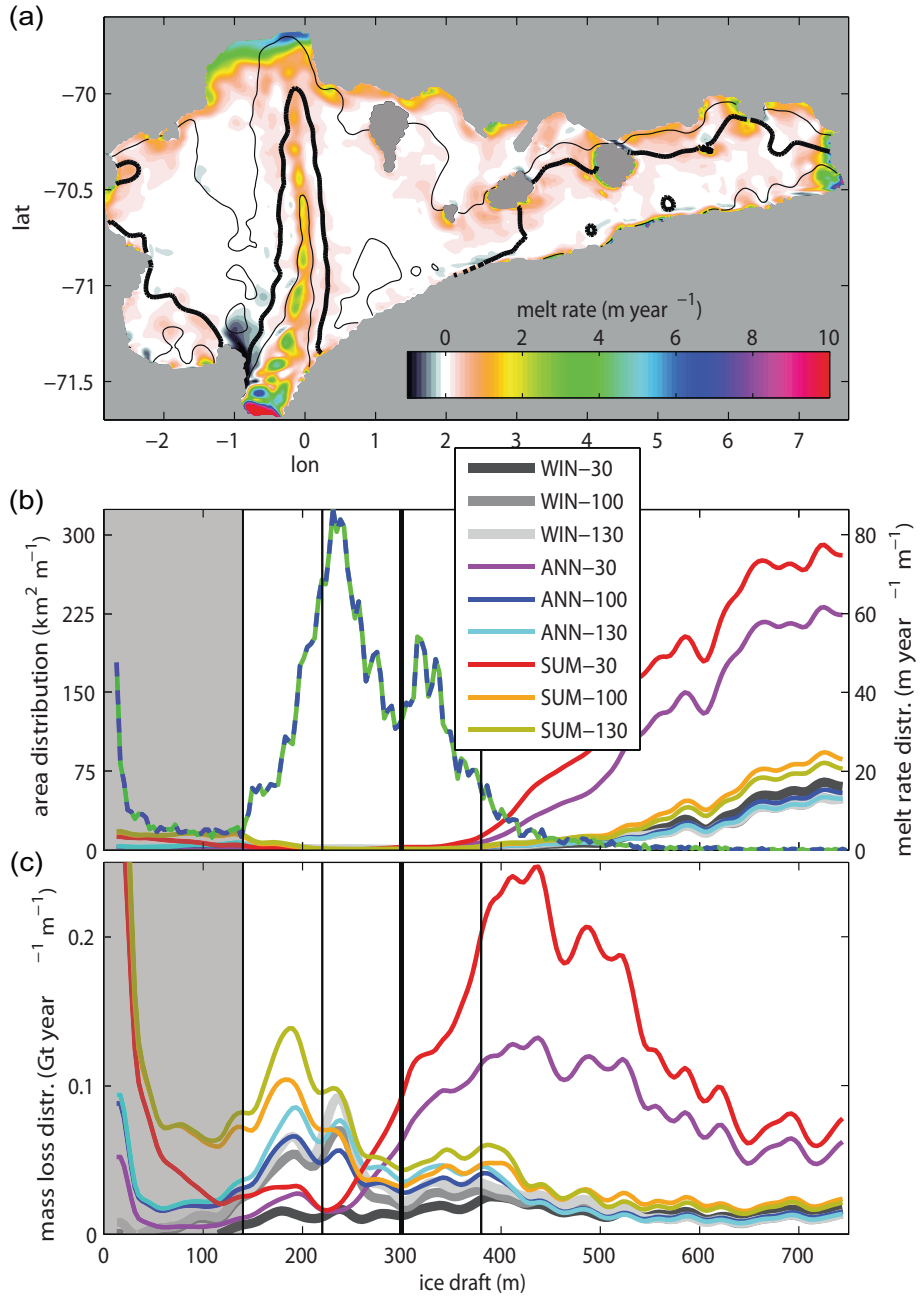

Fig. 7. Spatial distribution of average melt rates in the ANN-100 experiment (a), with black contours indicating 220 m, 300 m and 380 m ice draft thickness shown in Fig. 2. In panel (b), the depth-distributed mean melt rates for the different experiments (right axis) are shown together with the histogram of ice shelf area (dashed line, left axis) as a function of depth. The total melting contribution at respective ice draft–obtained by multiplying the ice area by the melt rate– is shown in panel (c). The black vertical lines indicate the depth of the contours shown in panel (a), with the transition between the shallow and deep ice indicated by the thick vertical line at 300 m. The gray shaded area in (b) and (c) shows the melting contribution at the smoothed ice front that is excluded from our analysis.

(c) show the vertical distribution of ice shelf area and the basal melting contribution in various experiments. While the details of the depth-dependent melting response to different model forcings will be discussed in Section 5.2, the histogram of horizontal ice shelf area as a function of depth,[2] shown by the dashed curve (left axis) in Fig. 7(b), reveals large areas of *shallow ice* at about 250 m depth and large areas of *deep ice* at about 350 m depth, with a natural separation at the local minimum of the curve at 300 m depth. As indicated by the thick 300 m contour in Fig. 7(a), this pronounced bimodal distribution reflects the difference between the thicker body of the eastern FIS and the Jutulstraumen keel, and the large area of shallow ice in the central and western part of the FIS.

Fig. 5 suggests that the melt rates within these two different portions of the FIS are controlled by the varying amounts of ASW and WDW that enter the cavity at different times of the year in the ANN-100 experiment. In addition to the synthetic mooring data in Fig. 5(a), Fig. 5(b) and (c) show daily time series of the spatially averaged contribution of deep melting below and shallow melting above 300 m depth (excluding the smoothed ice front above 140 m depth as described above), together with a time series

[2] The curve was computed by binning the total ice draft area, represented by the 1.5 km^2 × 1.5^2 model grid cells, into 200 equally spaced depth bins and normalizing the area in each bin with the vertical bin size of about 4 m. For clarity of the figure, the displayed distribution was smoothed with a 10 point Hanning-filter, such that the integrated area beneath the curve approximates the total ice shelf area in the model.

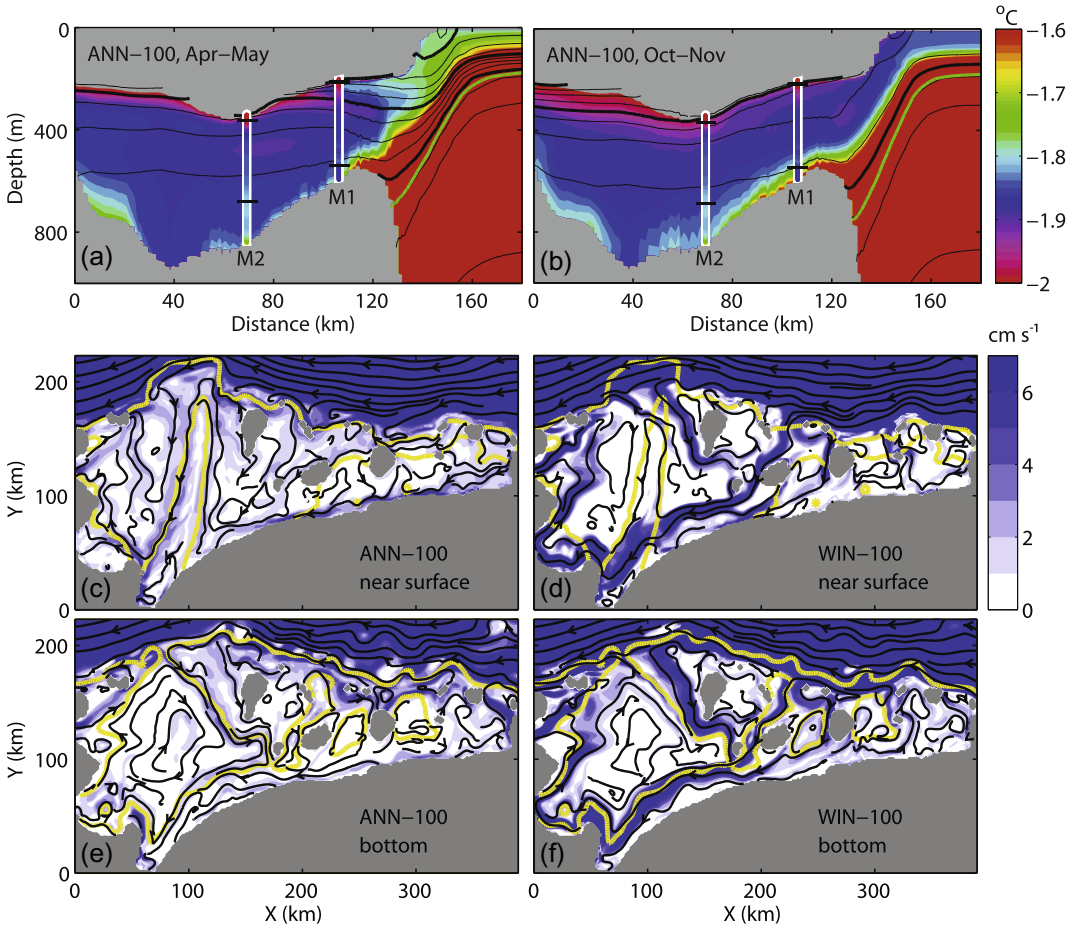

Fig. 8. An overview of the simulated cavity circulation. Upper panels show potential temperature (color shading) and density contours (black) for the seasonal extremes in late summer and fall (a) and late winter and spring (b) along the cross section indicated in Fig. 2. The −0.3 °C isotherm (green contour) indicates the southward deepening thermocline. Colored vertical lines in both panels show observed temperatures obtained from the CTD profiles in December 2010 at mooring locations M1 and M2, with black horizontal ticks indicating the respective depths of the mooring instruments. Panels (c) to (f) compare the cavity circulations in the ANN-100 (left column) and the WIN-100 (right column) experiments. The color shading shows current velocity in a layer near the ocean surface (upper row) and at the bottom (lower row) time-averaged over the last model year. Current directions are indicated by black flow contours, which are produced with the Matlab function 'streamslice' that approximates the particle trajectory in a steady circulation. Yellow contours show ice draft (140 m and 300 m) and water column thickness (350 m) for the upper and lower panels, respectively. (For interpretation of the references to color in this figure legend, the reader is referred to the web version of this article.)

of the potential temperature (color) and salinity (contours) profile at M1. Comparing the evolution of melt rates and water mass beneath the FIS shows that stronger melting of shallow ice from March to July coincides with periods when warm ASW enters the cavity near the surface, while stronger melting at depth from November to February is presumably caused by MWDW that eventually comes into contact with the deep ice after entering across the main sill between September and December. This seasonality of melting at different depths is consistent with the melting and freezing pattern that was inferred from the mooring data, with the model also reproducing the annual cycle of melting and refreezing of ISW near M1 (not shown) that was suggested by Hattermann et al. (2012).

The thickness distribution in Fig. 7(b) also shows a long tail of very deep ice below 400 m, mainly corresponding to the southern part of Jutulstraumen. While the map in Fig. 7(a) shows the largest melt rates in this region, Fig. 7(b) reveals that the high melting of deep ice only affects a small fraction of the total ice shelf area.

4.3. Ice shelf cavity circulation

The spatial pattern of water masses and the general circulation within the ice shelf cavity is shown in Fig. 8. The upper two panels show the seasonal extremes of ocean temperature along a cross-section beneath the ice shelf cavity (green line in Fig. 2(a)), obtained by time averaging the five years of the ANN-100 experiment for April and May in fall (Fig. 8(a)), and October and November in spring (Fig. 8(b)), respectively. Comparing the cross-sections shows two basic features of the seasonality that explain the melting variability seen in Fig. 5(b). Firstly, the seasonal inflow of ASW in the upper part of the cavity can be seen by the closely spaced isopycnals and higher temperatures (green color shading) extending from the ocean surface to beneath the ice shelf draft during the fall in Fig. 8(a). Although the ASW temperatures are only slightly above the surface freezing point, the surface water increases the thermodynamic forcing at the ice base, because it separates the ice from relatively denser ISW ascending from greater depth. This effect is shown in Fig. 8(a), where the cold ISW layer (magenta) detaches from the ice base at a distance approximately 10 km south of M1, as opposed to the spring season (Fig. 8(b)), where no ASW is present and a continuous layer of ISW extends all the way to the ice front. Secondly, the seasonal inflow of MWDW at depth is seen by the layer of relatively warm (green and red shading) waters extending from the offshore thermocline to M2 during the spring Fig. 8(b). This warm bottom layer is created by pulses of MWDW that flush across the main sill when the thermocline is

temporarily lifted above the sill depth by the internal (eddy-driven) variability of the coastal flow.

The seasonal pattern in Fig. 8(a) and (b) also shows that the ASW and the MWDW both reside for several months beneath the FIS, potentially affecting basal melting far inside the cavity. The MWDW, entering the cavity at the main sill in Fig. 8(b), is advected along topographic (f/H) contours further into the cavity, appearing as a warmer bottom layer (green) at the southernmost end of the cross-section in Fig. 8(a), and eventually causes melting of deep ice of Jutulstraumen. The evolution of the ASW, entering in the upper part of the cavity in Fig. 8(a), is shown by the thickened and more stratified layer of cold ISW (magenta) at the southern end in Fig. 8(b). A water mass analysis (not shown) reveals that the buoyant upper portion of this ISW layer is formed by surface water which entered the cavity during the previous summer and has expended its available heat for melting. Thus, our simulations confirm the hypothesis of Hattermann et al. (2012) that ASW can travel far into the ice shelf cavity, after initially being subducted beneath the ice front.

An overview of the horizontal current strength and direction is presented in the lower panels of Fig. 8. A dominant feature of the sub-ice shelf circulation is the presence of counter-rotating, topographically constrained flows in the upper and lower water column of the central basin. At depth, the model shows a clockwise flow steered by the bottom topography, while in the upper part of the water column a counter-clockwise flow along ice draft contours is observed. We find that the different circulation patterns in the upper and lower parts of the cavity are a direct result of the enhanced stratification due to the presence of ASW. This can be seen by comparing the results from the ANN-100 experiment (Fig. 8(c) and (e)) to the circulation in the initial simulation (Fig. 8(d) and (f)), which uses the WIN-100 forcing where no ASW is included in the model. In contrast to the vertically sheared currents described above, the constant winter scenario shows a narrow but fast-flowing, topographically steered barotropic jet, with much larger current speeds in the upper part of the water column than observed in the ANN-100 experiment. Also the seasonal variability in the ANN-100 experiment (not shown) reveals stronger and more barotropic sub-shelf currents near the ice base during late winter and spring when the upper ocean stratification is weak.

The analysis of the ANN-100 experiment thus, reveals several effects of ASW on the cavity ventilation and associated basal melting. In particular, the pronounced seasonality of the MWDW inflow at depth, which occurs in the absence of any variability of the wind forcing, is an interesting result implying a direct link between upper ocean hydrographic conditions and the deep ocean heat fluxes. In fact, without ASW in the model, no MWDW enters the cavity, as can be seen from the last six months of the constant winter initial simulation in Fig. 5(a).

5. Model response to alternate forcings

5.1. Two states of basal melting

By analyzing the depth-distributed contribution to the overall basal mass balance in various experiments, we isolate the melting contribution attributed to the different heat sources below the FIS. Along with the vertically binned ice shelf thickness distribution, Fig. 7(b) also shows the mean melt rates within each depth bin (right axis) for nine different experiments, corresponding to the strongest (130), weakest (30), and intermediate wind forcing (100) for each of the three different hydrographic scenarios, temporally averaged over the respective last model year. The results generally reflect the spatial pattern of Fig. 7(a), with high melt rates above 10 m year^{-1} only occurring at deep ice below 400 m, and melt rates of less than 1 m year^{-1} at ice depths between 200 m and 400 m for all experiments. Somewhat higher melt rates of up to 3 m year^{-1} also occur at locations of very shallow ice above 200 m depth, corresponding to enhanced melting near the ice front.

The contribution to the total basal mass balance within a given depth bin, obtained by multiplying the vertically binned mean melt rates by the ice shelf area distribution, is shown in Fig. 7(c), with three main features being evident from the graph.[3] Firstly, the deep and shallow melting respond in opposite ways to winds. Melting of shallow ice above 400 m increases with the strength of the wind forcing, whereas melt rates below 400 m are largest for the weakest winds for all hydrographic scenarios. Secondly, melting of both deep ice and shallow ice, are strongest in the constant summer scenario and weakest in the constant winter scenario for equal wind forcings. Thirdly and perhaps most noticeably, the melting response is strongly modulated by the uneven distribution of ice shelf area. In most experiments, the basal mass loss is dominated by weak melting of large areas of shallow ice, while substantial changes of the mass loss at very deep ice only occur for the extremely large deep melt rates in the ANN-30 and SUM-30 experiments shown in Fig. 7(c).

The characteristic depth-dependent melting response to varying forcing is summarized in Fig. 9(a) and (b). The colored curves are identical in both panels, showing the total amount of melting for the entire ice shelf as function of the wind forcing. The colored patches show the contribution of melting only from ice deeper than 300 m (Fig. 9(a)), or from melting at ice shallower than 300 m (Fig. 9(b)), respectively. For an applied surface stress above 60% of the climatological average (indicated by the vertical lines in Fig. 9), the melting response in all hydrographic scenarios is dominated by changes of the shallow melting contribution, which correlates roughly linearly with the applied surface stress (Fig. 9(b)). For weaker surface stress below 60% of the climatological average, in contrast, the melting response in the annual cycle and constant summer scenarios are dominated by the deep melting contribution which strongly increases for decreasing surface stress. These different dependencies of the deep and shallow melting on forcing variations suggests the classification of two separate states of melting at the FIS: (i) a state of shallow melting for stronger winds, in which the melting is controlled by small melt rate changes beneath large areas of shallow ice; and (ii) a state of deep melting for weaker winds, in which the overall basal mass loss is dominated by very high melt rates at small areas of deep ice. The transition between these two states of melting appears to be controlled by the combined effect of wind and hydrographic conditions. We now continue by analyzing the oceanic response to forcing variations in our model.

5.2. Oceanic controls on deep and shallow melting

In order to explain the effect of climatic forcing on basal melting, we investigate the oceanic changes in the different experiments, with the main mechanisms controlling the respective contribution of the deep and shallow melting depicted in Fig. 10. The deep ocean heat transport towards the ice is primarily controlled by the depth of the ASF thermocline relative to the continental shelf break. Comparing the time-averaged near-shore thermocline depth in Fig. 9(c) to the deep melting contribution in Fig. 9(a) shows that a transition towards the state of deep melting occurs when the WDW rises above the depth of the main sill

[3] Similar to the area distribution in Fig. 7(b), the depth distributed melting contribution is normalized and filtered, such that the integrated area below the curve approximates the total mass loss over the entire ice shelf base.

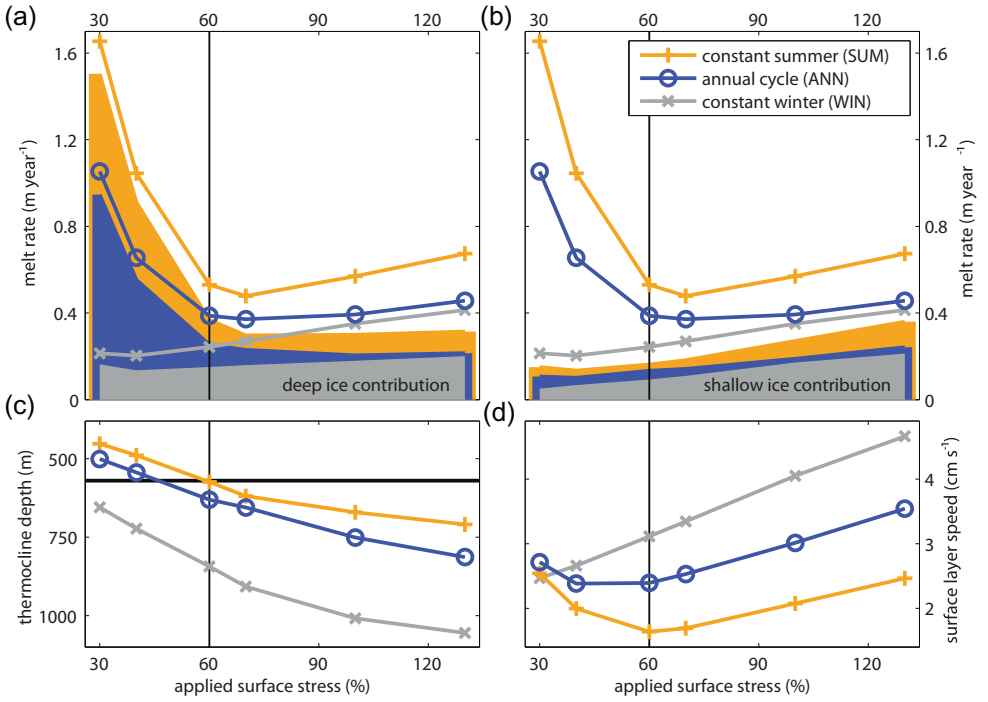

Fig. 9. The net basal melting of deep ice below 300 m depth and shallow ice between 140 m and 300 m depth as a function of wind forcing for the different hydrographic scenarios is shown by the colored patches in panels (a) and (b). The solid curves are identical in both panels, and show the total mass loss of the entire FIS. The different colors correspond to the different hydrographic scenarios. Panel (c) shows the depth of the ASF thermocline in the main sill area, with the sill depth indicated by the black horizontal line. Panel (d) shows the average current speed in the ocean surface layer below the shallow ice.

(horizontal line) for weaker wind forcing. Similarly a consistent response of the deep ocean heat transport is indicated by the simulated time series of the M1 temperature profiles in Fig. 5(c)–(e), and the modeled θ–S histograms in Fig. 6, which in the ANN-30 experiment show unmodified WDW inside the cavity.

While stronger wind forcing deepens the ESW layer near the coast, Fig. 9(c) shows that the presence of ASW in summer generally leads to a shallower thermocline position, promoting the transition into the state of deep melting for stronger winds. The apparent uplift of the thermocline for a more buoyant upper water column suggests a positive feedback (P6 in Fig. 10), in which glacial melt water release may increase the deep ocean heat transport by freshening the upper water column, leading to further melting. This model behavior agrees with the idea that the ASF is controlled by the balance between the wind-driven Ekman overturning and the counteracting eddy fluxes (Nøst et al., 2011). In this theory, stronger easterly winds deepen the thermocline due to increased coastal downwelling—indicated by the arrow denoted P1 in Fig. 10—while larger horizontal density gradients associated with the buoyant ASW are expected to lift up the thermocline (P2 in Fig. 10) by increasing the baroclinicity of the front and enhancing the eddy activity. However, some aspects of the deep melting response remain unexplained, such as the timing of the warm inflow at depth in the ANN-100 experiment. In this experiment, pulses of MWDW occurs primarily during times of the year when the least amount of ASW is present outside the ice shelf cavity and the seasonally varying thermocline depth reaches its deepest depth. Hence, the model suggests a more complicated interaction of the frontal processes with the cavity circulation, and a full investigation of this transient response to the time-varying forcing will need attention in future work.

The simulated melting beneath shallower parts of the FIS appears to be determined by the combined effect of sub-ice shelf currents and hydrography. For all hydrographic scenarios, stronger winds increase the shallow melting (P3 in Fig. 10), because a more

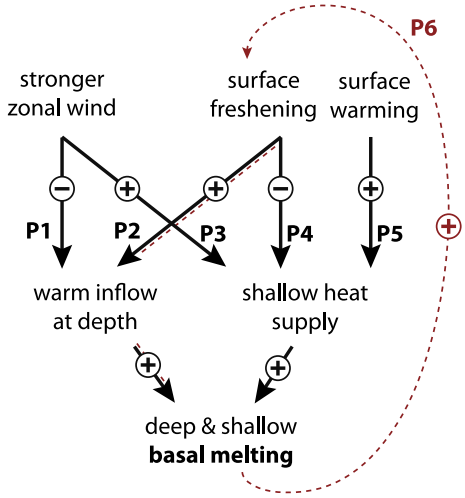

Fig. 10. A schematic that shows how varying surface stress and upper-ocean hydrography affect basal melting by increasing (+) and decreasing (−) the deep and shallow heat transport towards the ice. The different processes revealed by our simulations, denoted P1 to P5, are explained in Section 5.2. A possible self-amplifying feedback, in which the upper-ocean freshening due to basal melting enhances the deep ocean heat transport by lifting up the ASF thermocline, is denoted as P6.

energetic upper ocean circulation (Fig. 9(d)) enhances the exchange of ISW with warmer ambient water beneath the ice, and stronger currents also increase the parameterized mixing at the ice shelf/ocean boundary. Accordingly, the experiments with stronger winds show more surface water beneath the ice, indicated by the salinity contours on top of the temperature shading in Fig. 5(c)–(e), and the more frequent occurrence of buoyant water in the θ-S histograms in Fig. 6(d)–(f). The surface layer speeds in Fig. 9(d) also show stronger currents for the weak wind experi-

ments in the ANN- and SUM-scenarios that are not consistent with this theory. However, this is likely an internal melting feedback, where strong deep melting produces highly buoyant plumes that rise along the ice base and dominate the shallow flow field in these simulations.

The varying hydrographic conditions are found to have two opposite effects on the shallow melting response in the different experiments. One effect is that ASW increases the melt rates by replacing the cold ISW with warmer waters near the ice base as described in Section 4.3 (P5 in Fig. 10). The opposing effect is that larger amounts of buoyant surface water in the model reduce the shallow melting by weakening the near-surface currents (Fig. 9(d)), as demonstrated by comparing the circulation between the ANN-100 and the WIN-100 experiment in Fig. 8.

In order to separate the dynamic control of the ASW (P4 in Fig. 10) from its role as an additional heat source, an additional model experiment was conducted, in which the hydrographic forcing uses the constant summer scenario to restore the salinity, but applies the constant winter scenario with all waters above the thermocline at surface freezing-point for restoring the temperatures. The result is an upper-ocean circulation that is as weak as in the constant summer situation, and shallow melt rates that are even weaker than in the constant winter scenario. This shows that the density of ASW, being mainly controlled by salinity, can counteract the melting increase caused by warmer temperatures. A more detailed analysis (not shown) reveals that the weaker upper-ocean currents not only decrease the friction velocity in the applied basal melting parameterization, but also reduce the mixing of the ISW beneath the ice base with the (warmer) ambient water in the cavity.

6. Discussion

6.1. Ice shelf mass balance

Averaging over the ice shelf area of about 39,000 km^2 and assuming an ice density of 917 kg m^2, the ANN-100 simulation provides a basal mass loss of about 14 Gt $year^{-1}$, equivalent to a freshwater flux of roughly 0.5×10^{-3} Sv. This is a substantially lower estimate than obtained from previous modeling studies (Table 2), with implications for the overall mass budget of the ice shelf, which had been suggested to be decreasing based on model-derived melt rates (Smedsrud et al., 2006). The remote sensing based estimates of Rignot et al. (2013) yield a total mass flux of 25 Gt $year^{-1}$ feeding from the grounded ice sheet into the FIS, a mass loss at the calving front of 18 Gt $year^{-1}$, and a surface mass gain of 13 Gt $year^{-1}$, consistent with the recent ground-based observations suggesting an average surface mass balance of 300 kg m^{-2} for the FIS (Sinisalo et al., 2013). Our melting estimate is in much better agreement with the inferred steady-state melt rate of 20 Gt $year^{-1}$ than previous modeling results, supporting the findings of Rignot et al. (2013) and Pritchard et al. (2012) that the FIS is approximately in balance.

Table 2
Table of basal melting estimates at the FIS as obtained from ocean modeling studies, showing the simulated ice shelf area ($\times 10^3$ km^2), average basal melt rates BMR (m $year^{-1}$) and total basal mass loss BML (Gt $year^{-1}$). BML marked with (*) is computed based on the ice shelf area used in this study.

Study	Area	BMR	BML
This study, ANN-100	39	0.4	14
Hellmer (2004)	54	4.9	243
Smedsrud et al. (2006)	–	1.9	68*
Nicholls et al. (2008)	–	0.9	30*
Timmermann et al. (2012)	53	2.8	130
Rignot et al. (2013)	41	0.6	24

The magnitude and the general horizontal pattern of the simulated melt rates in the ANN-100 experiment also compare well with the results presented by Humbert (2010), who constrained basal melting from inverse ice flow modeling assuming a steady-state equilibrium ice shelf geometry. Although Humbert (2010) did not estimate the spatially-averaged basal mass loss, the agreement of our oceanic simulations with her melt rate distribution, which also depends on the idealized temperature structure applied in the ice flow model, suggests that a stable ice shelf geometry may indeed be a realistic assumption for the FIS.

6.2. The role of eddies and surface processes

Earlier, we argued for the importance of eddy processes for successfully simulating the heat transport towards the FIS. This hypothesis is supported by the resemblance of the observed intermittent, eddy-like pulses of MWDW for the ANN-100 experiment, in which all high-frequency variability stems from instabilities of the coastal current. But also the complex response of the ASF thermocline depth and deep ocean heat transport to varying oceanic forcing confirm the central role of eddy processes for basal melting at the FIS. While realistically parameterizing the effect of eddies over sloping topography is one of the greatest challenges for ocean models today (Isachsen, 2011), the idealized simulations in the related studies of Zhou et al. (2014) and Nøst et al. (2011) demonstrate the role of the eddy overturning in combination with winds for determining the depth of the thermocline along the Eastern Weddell Sea coast. Furthermore, the sensitivity tests in our study show that for a configuration near the transition between the deep and shallow states of melting, small errors in thermocline depth and bedrock topography may lead to significant changes in simulated melt rates.

Our study also emphasizes the role of ASW, both in serving as a direct heat source for melting, and by affecting the frontal dynamics along the Eastern Weddell Sea coast. The seasonal access of ASW beneath the FIS was first observed by Hattermann et al. (2012), and a similar seasonality of basal melting seen in the ANN-100 experiment was suggested by coarser model simulations using isopycnal coordinates (Nicholls et al., 2008). While the smoothed topography in ROMS may lead to an overestimate of upper ocean contribution to melting beneath the FIS, sensitivity studies with the idealized setup of Zhou et al. (2014) suggest that the inflow of ASW is indeed a realistic feature of the simulations. In their experiments with different ice shelf geometries, the amount of ASW entering the cavity is largely independent of the shape of the ice front, and occurs when the wind-driven deepening of the ASW layer outside the cavity exceeds the depth of the ice draft. Nevertheless, numerical artifacts associated with the terrain following coordinates cannot be ruled out in this setup. Quantifying the exact contribution of upper ocean Mode 3-type of melting, and scrutinizing its sensitivity to varying forcing, thus remains subject to future work.

The idealized simulations of Zhou et al. (2014) also show that the effect of the ASW on the frontal dynamics is a robust result and not an artifact of the hydrographic nudging at the periodic model boundary, a potential criticism in our model. Their annual experiments reproduce a similar deepening of the ASW and a shallower thermocline near the coast, although the ASW is exclusively introduced at the ocean surface.

6.3. Remaining issues

The realism of our simulations is challenged by the simplifications that are necessary to compromise the resolution of mesoscale eddies in a compact periodic domain, the limited amount of data available to construct the model forcing and boundary conditions,

and the desire to limit the model's complexity for the process-oriented sensitivity studies. Time-varying winds (Graham et al., 2013) and the modulating mechanical effect of sea ice (Nunez-Riboni and Fahrbach, 2009) are likely to modify the short-term and seasonal variability seen in the ANN-100 experiment. The effects of a reduced momentum transfer during the maximum sea ice extent in winter could possibly be inferred from the experiments with different constant wind forcings, but a main challenge will be to better understand the ambiguous role of sea ice during transition between fully ice-covered and open-water conditions (Lüpkes and Birnbaum, 2005). To investigate the effect of time-varying winds, we conducted an additional test run with the 6-hourly RACMO2 wind stress applied. Compared to the constant-wind scenario, this run shows more variability of the coastal current and enhanced deep and shallow melting by about 10 cm year^{-1} for the entire ice shelf. But this simulation also features more MWDW inside the ice shelf cavity than shown by the observations. While this run appears to overestimate the deep melting despite its seemingly more realistic forcing, it remains unclear to which degree the increased current variability causing the increased access of MWDW is a robust model result, or caused by artifacts introduced by interference of high frequency features at the cyclic boundaries.

Tides increase mixing near the ice base (Makinson and Nicholls, 1999) and their omission is likely to lead to underestimated melt rates in our study. A test with residual tidal velocity of 5 cm s^{-1}, obtained from spatially averaged results of the tidal model of Padman et al. (2002) for the parameterization of the heat flux at the ice base, showed a total melting increase of less than 5 cm year^{-1} compared to the ANN-100 experiment. However, non-linear tidal effects at the ice/ocean boundary (Makinson et al., 2011) may cause larger impacts. Tides may also enhance the frontal exchange at the shelf break (Padman et al., 2009), but these effects are expected to add only little to the ANN-100 melting estimate, because any additional inflow of warm water at depth due to tides would be seen in the M1 temperature time series near the main sill.

Another source of uncertainty relates to the idealized hydrographic forcing, which assumes a zonally uniform structure of the ASF with constant water masses below the thermocline and only low frequency (seasonal) variability of upper ocean properties. While this construction compromises the limited availability of observations and the insufficient representation of ASF-dynamics in large-scale ocean simulations, the results of Graham et al. (2013) highlight the importance of advection of upper-ocean hydrographic anomalies within the coastal current. Together with possible effects of deep ocean variability (Smedsrud, 2005), such transient effects of the coastal circulation will need to be included in more realistic simulations. Although dense water formation due to sea ice production is of minor importance in the Eastern Weddell Sea (Nicholls et al., 2009), also the effects of brine rejection and melt water release on the stratification of the coastal water column (Petty et al., 2013) are probably only partly captured by our approach of restoring surface properties to climatological values. However, including a dynamical sea ice component and parameterizations of the air/ice/sea interaction therein would further broaden the parameter space of our model, requiring additional validation (that would mainly rely on the seal data, which is now directly applied as a forcing), while the melt rate refinements would likely be small compared to the remaining uncertainties.

While these omitted processes may further complicate the ASF-dynamics, none of them are likely to change our main finding that the observed water masses beneath the FIS yield substantially less basal mass loss than suggested by previous models. Despite its simplifications, the ANN-100 simulation convincingly reproduces the sub-ice shelf observations, suggesting that the semi-idealized setup captures the main mechanisms controlling the heat transport towards the FIS. In particular, the limited inflow of WDW, causing the low melting estimate of our study, is a robust result that is confirmed by the observations. Taking into account the above-mentioned uncertainties due to the omission of tides and time-varying winds, we thus conclude that realistic melt rates are likely to range between our low-end estimate and the 0.9 m year^{-1} suggested by Nicholls et al. (2008), who simulated a comparable weak state of shallow melting in a coarse resolution model, but with more warm water entering the cavity.

7. Conclusion

This study presents the first high-resolution ocean circulation model of the Fimbul Ice Shelf (FIS) region in East Antarctica. For a simplified present-day forcing, the model reproduces recent sub-ice shelf observations and appears to capture the major dynamical processes of the slope front–continental shelf–ice shelf system.

The main lessons from the eddy-resolving simulations are as follows: (i) for the most realistic forcing, only small amounts of Modified Warm Deep Water (MWDW) enter beneath the FIS, suggesting relatively weak basal melting of about 0.4 m year^{-1} (14 Gt year^{-1}) and an ice shelf mass balance that is likely close to equilibrium; (ii) two distinct states of basal melting occur in the model, a shallow state and a deep state, controlled by different physical processes and in particular with opposing responses to wind stress forcing; and (iii) near-surface hydrographic conditions are important for modulating both the surface and the deep ocean heat fluxes.

The experiments with varying model forcing highlight the complex interplay between the three different modes of melting proposed by Jacobs et al. (1992). In the present state of shallow melting, the total basal mass loss is primarily controlled by upper ocean changes, emphasizing the relevance of the Mode 3-type of melting for the ice shelves in the Eastern Weddell Sea. The Mode 2-type of melting, due to warmer water at depth, only contributes significantly to the overall melting when the coastal thermocline rises above the main sill depth. But the intermittent inflow of MWDW that is presently observed may also be important because it determines the melt rates at deeper ice, which potentially affect the ice flow dynamics at the grounding line.

Our study explicitly focuses on the Eastern Weddell Sea region, where ice shelves are close to warm waters of open-ocean origin and continental shelf processes (such as sea ice formation) that add further complexity to the heat transport towards other ice shelves are of minor importance. However, some of our findings will also have implications for simulating basal melting in other regions of Antarctica. In particular, the role of mesoscale eddies in determining heat transport across oceanic fronts over the continental shelf break is a general result (Stewart and Thompson, 2013) that must be considered when assessing ice shelf basal melting in large scale oceanic simulations, such as the global warming studies of Hellmer et al. (2012) and Kusahara and Hasumi (2013). Also the modulating effect of the ice shelf thickness distribution on the melting response is a new finding that may help to better understand basal melting dynamics under other ice shelves. Finally, our results highlight the relevance of small-scale topographic features, which are still largely unknown beneath many ice shelves, for controlling the access of warm water into the ice shelf cavity.

Our work therefore emphasizes the need for further process-oriented studies, in conjunction with better observations of the Antarctic coastal dynamics, in order to improve and evaluate cli-

mate models and assess the present and future mass budget of the Antarctic Ice Sheet.

Acknowledgments

We thank Pål Erik Isachsen, Xylar Asay-Davis, Hartmut Hellmer and four anonymous reviewers for helpful comments that greatly improved the manuscript. We thank the German Space Agency (DLR) for providing via AO LAN0013 the TerraSAR-X imagery used by Angelika Humbert for detecting the location of ice rises, as well as Jan Lenaerts for providing the RACMO2 data. The seal data were derived from the IPY MEOP research programme; we thank Drs. Kit M. Kovacs, Martin Biuw, and Christian Lydersen for their respective roles in acquiring these data. This work was supported by the Centre for Ice, Climate, and Ecosystems (ICE) at the Norwegian Polar Institute and the NORKLIMA project 229764/E10 of Norwegian Research Council. The work of J.M. Lilly was supported by Physical Oceanography program awards #1235310 and #0849371 from the United States National Science Foundation.

Appendix A. Supplementary data

Supplementary data associated with this article can be found, in the online version, at http://dx.doi.org/10.1016/j.ocemod.2014.07.004.

References

Årthun, M., Nicholls, K.W., Makinson, K., Fedak, M.A., Boehme, L., 2012. Seasonal inflow of warm water onto the southern Weddell Sea continental shelf, Antarctica. Geophys. Res. Lett. 39 (17), L17601.

Abrahamsen, E.P., 2012. Oceanographic Conditions Beneath Fimbul Ice Shelf, Antarctica (Ph.D. thesis). University of Southampton.

Beckmann, A., Haidvogel, D.B., 1993. Numerical simulation of flow around a tall isolated seamount. Part I: Problem formulation and model accuracy. J. Phys. Oceanogr. 23 (8), 1736–1753.

Chavanne, C.P., Heywood, K.J., Nicholls, K.W., Fer, I., 2010. Observations of the Antarctic slope undercurrent in the southeastern Weddell Sea. Geophys. Res. Lett. 37 (L13601). http://dx.doi.org/10.1029/2010GL043603.

Dinniman, M., Klinck, J.M., Smith Jr., W.O., 2007. Influence of sea ice cover and icebergs on circulation and water mass formation in a numerical circulation model of the Ross Sea, Antarctica. J. Geophys. Res. 112 (C11013). http://dx.doi.org/10.1029/2006JC004036.

Dupont, T.K., Alley, R.B., 2005. Assessment of the importance of ice-shelf buttressing to ice-sheet flow. Geophys. Res. Lett. 32 (4), L04503.

Fraser, A.D., Massom, R.A., Michael, K.J., Galton-Fenzi, B.K., Lieser, J.L., 2012. East Antarctic landfast sea ice distribution and variability, 2000–08. J. Clim. 25 (4), 1137–1156.

Gade, H., 1979. Melting of ice in sea water: a primitive model with application to the Antarctic ice shelf and icebergs. J. Phys. Oceanogr. 9, 189–198.

Galton-Fenzi, B., 2009. Modelling Ice-Shelf/Ocean Interaction (Ph.D. thesis). University of Tasmania.

Galton-Fenzi, B.K., Hunter, J.R., Coleman, R., Marsland, S.J., Warner, R.C., 2012. Modeling the basal melting and marine ice accretion of the Amery Ice Shelf. J. Geophys. Res. 117 (C9), C09031.

Graham, J.A., Heywood, K.J., Chavanne, C.P., Holland, P.R., 2013. Seasonal variability of water masses and transport on the Antarctic continental shelf and slope in the southeastern Weddell Sea. J. Geophys. Res 118, 2201–2214.

Hattermann, T., Nøst, O.A., Lilly, J.M., Smedsrud, L.H., 2012. Two years of oceanic observations below the Fimbul ice shelf, Antarctica. Geophys. Res. Lett. 39 (12), L12605.

Hellmer, H.H., 2004. Impact of Antarctic ice shelf basal melting on sea ice and deep ocean properties. Geophys. Res. Lett. 31 (L10307). http://dx.doi.org/10.1029/2004GL019506.

Hellmer, H.H., Olbers, D.J., 1989. A two-dimensional model for the thermohaline circulation under an ice shelf. Antarct. Sci. 1 (04), 325–336.

Hellmer, H.H., Kauker, F., Timmermann, R., Determann, J., Rae, J., 2012. Twenty-first-century warming of a large Antarctic ice-shelf cavity by a redirected coastal current. Nature 485 (7397), 225–228.

Heywood, K.J., Locarnini, R.A., Frew, R.D., Dennis, P.F., King, B.A., 1998. Transport and water masses of the Antarctic slope front system in the eastern Weddell Sea. In: Jacobs, S.S., Weiss, R.F. (Eds.), Ocean, Ice and Atmosphere: Interactions at the Antarctic Continental Margin, Antarctic Research Series, vol. 75. American Geophysical Union, pp. 203–214.

Heywood, K.J., Garabato, A.C., Stevens, D.P., Muench, R.D., 2004. On the fate of the Antarctic slope front and the origin of the Weddell front. J. Geophys. Res. 109, C06021.

Holland, D.M., Jenkins, A., 1999. Modeling thermodynamic ice–ocean interactions at the base of an ice shelf. J. Phys. Oceanogr. 29 (8), 1787–1800.

Humbert, A., 2010. The temperature regime of Fimbulisen. Antarct. Ann. Glaciol. 51 (55), 56–64.

Humbert, A., 2012. Unpublished results from flux divergence calculations at Jutulstraumen Ice Stream. Personal communication via e-mail, September 2012.

Hunter, J.R., 2006. Specification for test models of ice shelf cavities. Tech. rep., Antarctic Climate and Ecosystems Cooperative Research Centre, Hobart, Australia.

Isachsen, P.E., 2011. Baroclinic instability and eddy tracer transport across sloping bottom topography: How well does a modified Eady model do in primitive equation simulations? Ocean Modell. 39 (1), 183–199. http://dx.doi.org/10.1016/j.ocemod.2010.09.007.

Jacobs, S.S., Hellmer, H.H., Doake, C.S.M., Jenkins, A., Frolich, R.M., 1992. Melting of Ice Shelves and the Mass Balance of Antarctica, vol. 38, pp. 375–387.

Jacobs, S.S., Jenkins, A., Giulivi, C.F., Dutrieux, P., 2011. Stronger ocean circulation and increased melting under Pine Island glacier ice shelf. Nat. Geosci. 4 (8), 519–523.

Jenkins, A., 1991. A one-dimensional model of ice shelf-ocean interaction. J. Geophys. Res. 96, 20671–20677.

Jenkins, A., 2011. Convection-driven melting near the grounding lines of ice shelves and tidewater glaciers. J. Phys. Oceanogr. 41 (12), 2279–2294.

Jenkins, A., Dutrieux, P., Jacobs, S.S., McPhail, S.D., Perrett, J.R., Webb, A.T., White, D., 2010. Observations beneath Pine island glacier in West Antarctica and implications for its retreat. Nat. Geosci. 3 (7), 468–472.

Joughin, I., Alley, R.B., Holland, D.M., 2012. Ice-sheet response to oceanic forcing. Science 338 (6111), 1172–1176.

Kusahara, K., Hasumi, H., 2013. Modeling Antarctic ice shelf responses to future climate changes and impacts on the ocean. J. Geophys. Res. 118 (5), 2454–2475.

Langley, K., von Deschwanden, A., Kohler, J., Sinisalo, A., Matsuoka, K., Hattermann, T., Humbert, A., Nøst, O.A., Isaksson, E., 2014. Complex network of channels beneath an Antarctic ice shelf. Geophys. Res. Lett. 41 (4), 1209–1215.

Langley, K., Kohler, J., Sinisalo, A., yan, M.J., Hamran, S.E., Hattermann, T., Isaksson, E., Matsuoka, K., Nøst, O.A., in preparation. Interferometric radar measures low melt rates with seasonality at the base of the Fimbul Ice Shelf, Antarctica.

Le Brocq, A.M., Ross, N., Griggs, J.A., Bingham, R.G., Corr, H.F.J., Ferraccioli, F., Jenkins, A., Jordan, T.A., Payne, A.J., Rippin, D.M., Siegert, M.J., 2013. Evidence from ice shelves for channelized meltwater flow beneath the Antarctic Ice Sheet. Nat. Geosci. 6 (11), 945–948.

Lenaerts, J.T.M., van den Broeke, M.R., van de Berg, W.J., van Meijgaard, E., Kuipers Munneke, P., 2012. A new, high-resolution surface mass balance map of Antarctica (1979–2010) based on regional atmospheric climate modeling. Geophys. Res. Lett. 39 (4), L04501.

Lilly, J.M., Olhede, S.C., 2009. Higher-order properties of analytic wavelets. IEEE Trans. Signal Process. 57 (1), 146–160.

Lilly, J.M., Rhines, P.B., Schott, F., Lavender, K., Lazier, J., Send, U., D'Asaro, E., 2003. Observations of the Labrador Sea eddy field. Prog. Oceanogr. 59 (1), 75–176.

Losch, M., 2008. Modeling ice shelf cavities in a z coordinate ocean general circulation model. J. Geophys. Res. 113 (10.1029).

Lüpkes, C., Birnbaum, G., 2005. Surface drag in the Arctic marginal sea-ice zone: a comparison of different parameterization concepts. Bound.-Layer Met. 117, 179–211.

Makinson, K., Nicholls, K.W., 1999. Modeling tidal currents beneath Filchner–Ronne ice shelf and on the adjacent continental shelf: their effect on mixing and transport. J. Geophys. Res. 104 (C6), 13449–13465.

Makinson, K., Holland, P.R., Jenkins, A., Nicholls, K.W., Holland, D.M., 2011. Influence of tides on melting and freezing beneath Filchner–Ronne ice shelf, Antarctica. Geophys. Res. Lett. 38 (6). http://dx.doi.org/10.1029/2010GL046462.

Mercer, J., 1978. West Antarctic ice sheet and CO_2 greenhouse effect: a threat of disaster. Nature 27, 26.

Nicholls, K.W., Abrahamsen, E.P., Buck, J.J., Dodd, P.A., Goldblatt, C., Griffiths, G., Heywood, K.J., Hughes, N.E., Kaletzky, A., Lane-Serff, G.F., McPhail, S.D., Millard, N.W., Oliver, K.I.C., Perrett, J., Price, M.R., Pudsey, C.J., Saw, K., Stansfield, K., Stott, M.J., Wadhams, P., Webb, A.T., Wilkinson, J.P., 2006. Measurements beneath an Antarctic ice shelf using an autonomous underwater vehicle. Geophys. Res. Lett. 33 (L08612). http://dx.doi.org/10.1029/2006GL025998.

Nicholls, K.W., Abrahamsen, E.P., Heywood, K.J., Stansfield, K., Østerhus, S., 2008. High-latitude oceanography using autosub autonomous underwater vehicle. Limnol. Oceanogr. 53 (5), 2309–2320.

Nicholls, K.W., Østerhus, S., Makinson, K., Gammelsrd, T., Fahrbach, E., 2009. Ice–ocean processes over the continental shelf of the southern Weddell Sea, Antarctica: a review. Rev. Geophys. 47, 23.

Nøst, O.A., 2004. Measurements of ice thickness and seabed topography under the Fimbul ice shelf, Dronning Maud Land, Antarctica. J. Geophys. Res. 109, C10010. http://dx.doi.org/10.1029/2004JC002277.

Nøst, O.A., Lothe, T., 1997. The Antarctic coastal current – physical oceanographic results from NARE 1996/97. In: Winther, J.G. (Ed.), Norsk Polarinstitutt Meddelelser, vol. 148. Norsk Polarinstitutt, pp. 51–57.

Nøst, O.A., Biuw, M., Tverberg, V., Lydersen, C., Hattermann, T., Zhou, Q., Smedsrud, L.H., Kovacs, K.M., 2011. Eddy overturning of the Antarctic slope front controls glacial melting in the eastern Weddell Sea. J. Geophys. Res. 116, C11014. http://dx.doi.org/10.1029/2011JC006965.

Nunez-Riboni, I., Fahrbach, E., 2009. Seasonal variability of the Antarctic coastal current and its driving mechanisms in the Weddell Sea. Deep-Sea Res. Part I 56, 1927–1941.

Ohshima, K.I., Takizawa, T., Ushio, S., Kawamura, T., 1996. Seasonal variations of the Antarctic coastal ocean in the vicinity of Lützow–Holm Bay. J. Geophys. Res. 101 (C9), 20617–20628.

Padman, L., Fricker, H.A., Coleman, R., Howard, S., Erofeeva, L., 2002. A new tide model for the Antarctic ice shelves and seas. Ann. Glaciol. 34 (1), 247–254.

Padman, L., Howard, S.L., Orsi, A.H., Muench, R.D., 2009. Tides of the northwestern Ross Sea and their impact on dense outflows of Antarctic bottom water. Deep-Sea Res. Part II 56 (13–14), 818–834.

Petty, A.A., Feltham, D.L., Holland, P.R., 2013. Impact of atmospheric forcing on Antarctic continental shelf water masses. J. Phys. Oceanogr. 43 (5), 920–940.

Price, M.R., Heywood, K.J., Nicholls, K.W., 2008. Ice-shelf–ocean interactions at Fimbul ice shelf, Antarctica from oxygen isotope ratio measurements. Ocean Sci. 4, 89–98.

Pritchard, H.D., Ligtenberg, S.R.M., Fricker, H.A., Vaughan, D.G., van den Broeke, M.R., Padman, L., 2012. Antarctic ice-sheet loss driven by basal melting of ice shelves. Nature 484 (7395), 502–505.

Rignot, E., Casassa, G., Gogineni, P., Rivera, A., Thomas, R., 2004. Accelerated ice discharge from the Antarctic Peninsula following the collapse of Larsen B ice shelf. Geophys. Res. Lett. 31. http://dx.doi.org/10.1129/2004GL020697.

Rignot, E., Bamber, J.L., van den Broeke, M.R., Davis, C., Li, Y., van de Berg, W.J., van Meijgaard, E., 2008. Recent Antarctic ice mass loss from radar-interferometry and regional climate-modelling. Nat. Geosci. 1 (2), 106–110.

Rignot, E., Jacobs, S., Mouginot, J., Scheuchl, B., 2013. Ice-shelf melting around Antarctica. Science 341 (6143), 266–270.

Scambos, T., Hulbe, C., Fahnestock, M., Bohlander, J., 2000. The link between climate warming and break-up of ice shelves in the Antarctic Peninsula. J. Glaciol. 46, 516–530.

Shchepetkin, A.F., McWilliams, J.C., 2005. The regional ocean modeling system (ROMS): a split-explicit, free-surface, topography-following coordinates ocean model. Ocean Modell. 9, 347–404.

Sinisalo, A., Anschütz, H., Aasen, A.T., Langley, K., von Deschwaden, A., Kohler, J., Matsuoka, K., Hamran, S.-E., Øyan, M.-J., Schlosser, E., Hagen, J.O., Nøst, O.A., Isaksson, 2013. Surface mass balance on Fimbul ice shelf, East Antarctica: comparison of field measurements and large-scale studies. J. Geophys. Res. 118 (20), 11,625–11,635.

Smedsrud, L.H., 2005. Warming of the deep water in the Weddell Sea along the Greenwich meridian: 1977–2001. Deep-Sea Res. Part I 52 (2), 241–258.

Smedsrud, L.H., Jenkins, A., Holland, D.M., Nøst, O.A., 2006. Modeling ocean processes below Fimbulisen, Antarctica. J. Geophys. Res. 111 (C01007). http://dx.doi.org/10.1029/2005JC002915.

Smith, S.D., 1988. Coefficients for sea surface wind stress, heat flux, and wind profiles as a function of wind speed and temperature. J. Geophys. Res. 93 (C12), 15,467–15,472.

Spreen, G., Kaleschke, L., Heygster, G., 2008. Sea ice remote sensing using AMSR-E 89-GHz channels. J. Geophys. Res. 113, 14.

Stewart, A.L., Thompson, A.F., 2013. Connecting Antarctic cross-slope exchange with southern ocean overturning. J. Phys. Oceanogr. 43 (7), 1453–1471.

St-Laurent, P., Klinck, J.M., Dinniman, M.S., 2013. On the role of coastal troughs in the circulation of warm circumpolar deep water on Antarctic ice shelves. J. Phys. Oceanogr. 43 (1), 51–64. http://dx.doi.org/10.1175/JPO-D-11-0237.1.

Sverdrup, H.U., 1953. The currents off the coast of Queen Maud Land. Norsk Geografisk Tidsskrift 14, 239–249.

Timmermann, R., Le Brocq, A., Deen, T., Domack, E., Dutrieux, P., Galton-Fenzi, B., Hellmer, H., Humbert, A., Jansen, D., Jenkins, A., Lambrecht, A., Makinson, K., Niederjasper, F., Nitsche, F., Nøst, O.A., Smedsrud, L.H., Smith, W.H.F., 2010. A consistent data set of Antarctic ice sheet topography, cavity geometry, and global bathymetry. Earth Syst. Sci. Data 2, 261–273.

Timmermann, R., Wang, Q., Hellmer, H., 2012. Ice shelf basal melting in a global finite-element sea ice – ice shelf – ocean model. Ann. Glaciol. 53 (60).

Tverberg, V., Nøst, O.A., 2009. Eddy overturning across a shelf edge front: Kongsfjorden, west Spitsbergen. J. Geophys. Res. 114 (C04024). http://dx.doi.org/10.1029/2008JC005106.

Walkden, G.J., Heywood, K.J., Nicholls, K.W., Abrahamsen, P., 2009. Freshwater transport at Fimbulisen. Antarct. J. Geophys. Res. 114 (C8), C08014.

Zhou, Q., Hattermann, T., Nøst, O.A., Biuw, M., Kovacs, K.M., Lydersen, C., 2014. Wind-driven spreading of freshwater beneath the ice shelves in the eastern Weddell Sea. J. Geophys. Res. 119. http://dx.doi.org/10.1002/2013JC009556.